

Review

Substituted Hydroxyapatite, Glass, and Glass-Ceramic Thin Films Deposited by Nanosecond Pulsed Laser Deposition (PLD) for Biomedical Applications: A Systematic Review

Roberto Teghil , Mariangela Curcio *  and Angela De Bonis * 

Dipartimento di Scienze, Università della Basilicata, Via dell'Ateneo Lucano 10, 85100 Potenza, Italy; roberto.teghil@unibas.it

* Correspondence: mariangela.curcio@unibas.it (M.C.); angela.debonis@unibas.it (A.D.B.)

Abstract: The deposition of thin films of bioactive materials is the most common approach to improve the bone bonding ability of an implant surface. With this purpose, several wet and plasma assisted deposition methods were proposed in the scientific literature. In this review, we considered films obtained by nanosecond Pulsed Laser Deposition (PLD). Since hydroxyapatite (HA) has composition and structure similar to that of the mineral component of the bone, the initial studies focused on the selection of experimental conditions that would allow the deposition of films that retain HA stoichiometry and crystallinity. However, biological apatite was found to be a poorly crystalline and multi-substituted mineral; consequently, the attention of researchers was oriented towards the deposition of substituted HA, glass (BG), and glass-ceramic (BGC) bioactive materials to exploit the biological relevance of foreign ions and crystallinity. In this work, after a description of the nanosecond ablation and film growth of ceramic materials, we reported studies on the mechanism of HA ablation and deposition, evidencing the peculiarities of PLD. The literature concerning the PLD of ion substituted HA, BG, and BGC was then reviewed and the performances of the coatings were discussed. We concluded by describing the advantages, limitations, and perspectives of PLD for biomedical applications.

Keywords: substituted hydroxyapatite; bioactive glass; bioactive glass-ceramic; PLD



Citation: Teghil, R.; Curcio, M.; De Bonis, A. Substituted Hydroxyapatite, Glass, and Glass-Ceramic Thin Films Deposited by Nanosecond Pulsed Laser Deposition (PLD) for Biomedical Applications: A Systematic Review. *Coatings* **2021**, *11*, 811. <https://doi.org/10.3390/coatings11070811>

Academic Editor: Gedvilas Mindaugas

Received: 4 June 2021

Accepted: 1 July 2021

Published: 4 July 2021

Publisher's Note: MDPI stays neutral with regard to jurisdictional claims in published maps and institutional affiliations.



Copyright: © 2021 by the authors. Licensee MDPI, Basel, Switzerland. This article is an open access article distributed under the terms and conditions of the Creative Commons Attribution (CC BY) license (<https://creativecommons.org/licenses/by/4.0/>).

1. Introduction

With increasing life expectancy, diseases connected to hard tissue, both bone and dental, can compromise the quality of life. Extraordinary progresses have been made in hard tissue health over the last decades, improving the mechanical properties, biocompatibility, and bioactivity of implants. Materials that can be used as implants offer controlled interaction with the biological medium, while also supporting and regenerating the damaged tissue, controlling specific biological reactions. Bioactive ceramics meet most of these needs; however, their brittleness limits application in load-bearing implants. Therefore, they are usually proposed as a coat for metal alloys, resulting in bioactive implants with suitable mechanical properties. Bioactive ceramic coatings on metallic implants can promote rapid bone fixation of the devices by enhancing bone growth and creating a strong interface; they can also act as a protective barrier, minimizing or preventing metallic ions release and reducing the risk of corrosion. Bioactive ceramics are inorganic, non-metallic, solid materials consisting of metal, non-metal, or metalloid atoms, with interatomic bonding (ionic or covalent), which is generally synthesized at elevated temperatures. The crystallinity of ceramic materials ranges from highly oriented to semi-crystalline, vitrified, and often completely amorphous (e.g., glass). Calcium phosphate-based minerals like hydroxyapatite (HA), bioactive glass (BG), and glass-ceramic (BGC) belong to the class of biomaterials suitable for hard tissue replacement.

Calcium phosphate-based minerals, especially hydroxyapatite (HA), resemble the main component of human hard tissues and have been proposed in the field of bone regeneration owing to their good biocompatibility, osseointegration, and osteoconduction [1–3]. The unit cell of HA is represented as $\text{Ca}_{10}(\text{PO}_4)_6(\text{OH})_2$. HA can easily accommodate ionic substitutes, retaining its crystal structure; and many studies have reported the synthesis and deposition of films of HA doped with microelements to give various metabolic functions to the coatings. The most common foreign ions that can be accommodated in the unit cell of HA are CO_3^{2-} in the position of PO_4^{3-} , Cl^- and F^- in the position of OH^- and Mg^{2+} , and Na^+ and K^+ in the position of Ca^{2+} , respectively. Researchers have also proposed the preparation of HA doped with ions that have functional properties, such as silver or iron [2,4–6]. The bacteriostatic and antibacterial activity of Cu, Ag, and Zn are well known and their accommodation in HA lattice is widely studied (the formation of bacterial biofilms in the first hours after surgery can accelerate implant failure). Bioactive and biocompatible coatings that possess antimicrobial activity have made it possible to improve surgical results and obviate the needs for antibiotics [7]. The use of Fe-doped HA has also been proposed, thanks to the intrinsic magnetic and biocompatibility properties of iron. It has been shown that the magnetic field can affect cell response and the incorporation of magnetic nanoparticles can create a magnetic gradient that influences cells behavior [8].

Considering glass materials, 45S5 Bioglass[®] was the first synthetic material able to bond with bone. Developed in the late 1960s by Larry Hench, Bioglass[®] has been in clinical use since 1985. It is a soda–lime–phosphosilicate ($\text{Na}_2\text{–CaO–P}_2\text{O}_5\text{–SiO}_2$) glass and the formula 45S5 has a specific meaning: 45 wt % S, which stands for SiO_2 (network former), and 5:1 is the ratio of $\text{CaO:P}_2\text{O}_5$ [9]. What traditional glass and bioactive glasses have in common is their amorphous structure and thermal behavior [10]. However, three important features distinguish bioactive glasses from traditional soda-lime-silica glasses: (i) less than 60 mol% SiO_2 ; (ii) high Na_2O and CaO percentage; (iii) high $\text{CaO/P}_2\text{O}_5$ ratio. Like hydroxyapatite, the composition of bioactive glasses is changing; in fact, in order to improve biological performances, numerous ions have been introduced. As regards the bioactive glass structure, there are three peculiar components to be taken into account: network formers, network modifiers, and intermediate oxides. Network formers, typically three or fourfold coordinated, include silica (SiO_2) and phosphorus pentoxide (P_2O_5). The basic building block of silicate glasses is the SiO_4^{4-} tetrahedron; each one can be connected to neighboring SiO_4^{4-} tetrahedrons through Si–O–Si bonds, named bridging oxygen atoms (BO). However, the presence of network modifiers varies the glass structure by the conversion of bridging oxygen atoms, with the predominant covalent character of the bond, into non-bridging oxygen atoms (NBO), with the predominant ionic character of Si–O– M^+ (where M^+ is a modifier cation) [11]. Network modifiers are, generally, the oxides of alkali or alkaline-earth metals, such as sodium, calcium, or strontium [12,13]. Finally, intermediate ions, such as Mg, Zn, Co, and Ni ions may reduce the tendency of the glass to crystallize, improving the bioactivity of the glass. However, it is difficult to predict their behavior because they can act like network modifiers or, if they enter the backbone of the glass structure, they can act more like network formers [14]. In any case, in order to ensure good bioactivity of the glass, the Si–O–Si/Si–O–NBO ratio should be ~ 1 [15].

A glass-ceramic is a glass containing micro- and nanocrystalline phases. There is no normative that determines the type of composition definable as glass-ceramic. Ravaglioli et al. [16] defined glass-ceramics as a glass that contains 1% to 80% (*v/v*) of crystalline phases. In the development of bioactive glasses, it has been demonstrated that bioactive glass, with composition suitable to obtain glass-ceramic, if annealed to create crystalline phases, can retain its bioactivity [17]. This was an important discovery in the improvement of the mechanical properties of bioactive glass. Various compositions based on silicate glass-ceramics have been since developed.

The reaction mechanism that characterizes the bioactivity of these materials is different for each kind of bioceramics; however, all of them have in common the ions exchange

between the material surfaces and the extracellular matrix, the adhesion of proteins and cells, the formation of a biological hydroxyapatite layer, and thus the osteointegration.

The features and properties of the deposited films depend on both the chosen bioceramics and the deposition technique. A wide range of bioceramics—from calcium phosphates to bioactive glass and glass-ceramics—are eligible.

The manufacture of high-quality coating is a complex issue; therefore, careful attention has to be paid to the optimization of the deposition parameters to ensure chemical and structural stability of the coating. The choice of material and deposition technique should be a balance of the most critical characteristics, collected below:

- **Crystallinity:** The presence of amorphous phases, which exhibit higher solubility in an aqueous medium, is desirable to accelerate bone formation. However, a too high dissolution rate compromises stability and increases the risk of failure. Consequently, crystalline phases are necessary to ensure term stability of the implant in clinical use [18]. Therefore, to prepare implants with predictable properties, it is necessary to design and control the crystallinity and purity of the coatings.
- **Surface topography:** The denser the microstructure of the coating is, less is its cracking or degradation. However, rough, textured, and porous surfaces could stimulate cell attachment and formation of an extra-cellular matrix. In particular, the combination of sub-microscale surface roughness, with microscale and nanoscale features, can stimulate both the adhesion of proteins involved in the regulation of osteoblast proliferation, and the adhesion and differentiation of cells [19,20]. Optimum coating porosity and roughness are important for in-growth of bone cells; conversely, the accumulation of macropores at the substrate/coating interface leads to a weakening of the coating adhesion.
- **Mechanical properties:** Good adhesion, high hardness, and high toughness are necessary to decrease residues generated during the functional loadings, which can be dangerous for the organism, and to prevent mechanical failures under load conditions [21].

Numerous techniques have been proposed to deposit bioactive films; they can be grouped into “wet methods”, such as sol-gel [22,23], electrophoretic deposition [24], electrochemical deposition [25], and plasma-assisted methods.

Among the physical deposition methods, Plasma Spray (PS) is the only method accepted to deposit HA films suitable for clinical trials [26,27]. In spray techniques, melted material is directed at a high speed on a surface where the melted particles rapidly solidify. PS is a low cost, high deposition rate technique, but it presents some problems, such as alteration in the HA structure, poor adhesion between coatings and metallic substrates due to the presence of tensile stress, and the tendency to crack and form debris [3,28].

Among alternative physical deposition techniques, Ion Beam Assisted Deposition (IBAD), Radio Frequency Magnetron Sputtering (RF-MS), and Pulsed Laser Deposition (PLD) are frequently proposed to create biocompatible films with interesting morphological and mechanical properties that can overcome the limits of PS-coated implants. The IBAD process is based on the combination of ion bombardment and physical vapor deposition with the presence of a specific energy ion beam directed at the substrate surface during the deposition. Bioactive films deposited by IBAD have high adhesion strength, since ion bombardment result in an atomic intermixed zone between the coating and the substrate surface [29–31], whereas the films’ crystallinity can be controlled by manipulating the substrate temperature during deposition. The formation of cracks in the deposited films were observed for the heat-treated samples due to the thermal expansion mismatch between the coated layer and the metal substrate [31]. RF-MS allows to coat implantable devices with films of uniform thickness [32]. Its deposition rate is strongly influenced by the target density and crystallinity, as was demonstrated during the deposition of Sr and Mg-doped β -TCP [33]. With regard to the coatings’ morphology, rough and smooth films can grow on the same substrate by varying the deposition parameters [34].

PLD is considered a very flexible technique since, with this method, it is possible to ablate targets with complex stoichiometry and obtain films with controlled thickness,

composition, texture, and morphology by varying several deposition parameters. Calcium phosphate-based coatings obtained by PLD present good mechanical performance, such as adhesion strength and hardness and, compared to RF-MS films, a rougher surface. All these properties could be beneficial in improving the films' bioactivity [35]. One of the advantages of PLD is the possibility to deposit doped HA films from a target obtained by the mixing of HA and metals or salt of the selected elements [36–38] in an eco-sustainable strategy that allows to avoid the high temperatures required with the wet synthetic approach. More recently, composite HA/biomolecules coatings were obtained by Matrix Assisted Pulsed Laser Evaporation (MAPLE), a “softer” ablation method that allows to deposit thin films, preserving the integrity of the biomolecules. HA films obtained by PLD have superior properties in terms of Ca/P ratio and morphology, but MAPLE is a very useful deposition method to tune HA surface with specific functionalities, immobilizing organic or bio-organic molecules and obtaining implants able to locally deliver drugs [39,40].

The typical advantages and limitations of the most frequently proposed deposition methods are reported in some reviews [3,28,34] and provided in Table 1.

Table 1. The most frequently used plasma-assisted deposition techniques to deposit bioactive ceramic films.

Deposition Technique	Advantages	Drawbacks	Ref.
PS	Low cost, high deposition rate	Poor adhesion, tendency to form cracks and debris, hard control of phase composition and surface morphology, delamination during implantation	[3,26–28,34]
RF-MS	Uniform thickness, controllable surface roughness	Low deposition rate, expensive	[3,28,32–34]
IBAD	High adhesion, homogeneous coatings	Cracks, expensive	[3,28–31,34]
MAPLE	Deposition of hybrid and thermal sensitive materials, accurate control of thickness, uniform coatings	Line of sight technique, low deposition rate	[39,40]
PLD	Films with complex stoichiometry, good adhesion and mechanical properties, controllable crystallinity, surface roughness and thickness	Low deposition rate, possibility of splashing or particles deposition	[3,28,34–38]

The aim of the current review is to have a bird's eye view on the state of the art of the fabrication of ion-substituted HA, BG, and BGC thin films. We have considered studies that report the deposition of bioactive films using the PLD technique, only. In recent years, the possibility to use biogenic sources to obtain calcium phosphate materials has been proposed by many authors, due to the similarity of these sources with hard tissues in terms of composition and crystallinity. However, we decided to not consider these studies in this paper since a review reporting recent advances in the deposition of biogenic HA was recently published [41].

2. Nanosecond PLD: Laser Ablation and Film Growth

Pulsed laser ablation is based on the interaction between a pulsed laser beam and the surface of solid target material. The ablation mechanism is strongly affected by laser pulse duration. Laser sources in the fs-ps time regime have been proposed for the ablation and deposition of oxides, carbides, and borides [42] whereas ceramics and glass ceramics bioactive films have been deposited only by nanosecond laser sources, to the best of our knowledge. During the interaction with a nanosecond laser, the target material absorbs the laser photon and in few ps, the energy is transferred to the electronic system directly, if the material is metallic, or to the lattice in non-metallic systems. The absorption process is followed by the thermal diffusion process, which leads to vaporization and plasma

formation during pulse time [43]. The laser-induced plasma is highly ionized, electrically neutral, and composed of atoms, molecules, ions, electrons, and clusters.

The heating of the target begins within the penetration depth of the material and is fast and strong [44]. This suggests that all target components evaporate at the same time, irrespective of their binding energy. As a matter of fact, the congruent evaporation of a multi-elemental target occurs only if the thermal diffusion length, depending on the thermal diffusion constant of the target and the laser pulse duration, is higher than the penetration depth. Consequently, laser-matter interaction is a very complex process, strongly dependent on pulse duration, laser wavelength and energy, and physico-chemical properties of the target material.

Following the well-known model of Miotello and Kelly [45,46], the interaction of a nanosecond pulsed laser beam with a material can be described by phase explosion, where superheated liquid undergoes a transition to a mixture of vapour and liquid droplets. When the target material has a large optical penetration depth (as ceramics), the fragmentation mechanism, as proposed by Perez [47], also has to be considered.

During the ablation in ns regime, the plasma interacts with the laser beam, mainly by inverse Bremsstrahlung [43,44,48]. The expansion of the plasma in vacuum is approximately adiabatic [43] and considered an ellipsoid [49]. In fact, the plasma expands in the three spatial directions, but preferentially along the direction perpendicular to the target surface, because there is a strong difference in pressure gradients in the axial and radial directions. The plume expansion dynamic in vacuum was extensively investigated by Anisimov et al. [49]. They considered the plume expansion similar to the expansion of an elliptical, neutral gas cloud. At the beginning of the expansion, the plume energy was considered purely thermal, and progressively transformed into kinetic energy during the expansion. When all the initial thermal energy is transferred to kinetic energy of the ablated species, free-plume expansion stage is reached, therefore, the plume front dynamics becomes linear with respect to time, reaching a maximum, asymptotic expansion velocity, typically in order of 10^6 cm/s [49]. These models describe pretty well the angular distribution of the ablated material, which can be fitted to a $\cos^n(\theta)$ [4], where n takes into account the anisotropy of the plasma distribution.

The first species of the plume, which arrive on the substrate surface after the first laser pulse, nucleate in subcritical clusters. These clusters dissociate in mobile species, which can nucleate in new clusters of different sizes. After the following pulse, the same process reoccurs and the only difference is that some of the incoming mobile species can join the clusters nucleated in the previous pulse. This process repeats for each laser pulse.

During the film's growth, several parameters affect its structure and morphology. Usually, a film deposited by nanosecond PLD is characterized by particulates embedded in the film; however, by tuning of the substrate-target distance, substrate temperature, laser fluence, and pressure in the ablation chamber, it is possible to control the particle size, or even avoid their presence on the film surface if a flat surface is required. Since film coating hard tissue implants require a rough surface, nano- and micron-size particles benefit the performances of the implant [19,20].

Since there are three main mechanisms of particulate production, strongly dependent on the target material and its near-surface morphology (condensation from vapour phase, target fragmentation and droplet ejection), particles that originated from different mechanisms can coexist in the same film [50].

Ultrafine particles originate by vapour phase (or gas-phase) condensation. Their dimension can be controlled by gas ambient pressure. In a typical PLD experiment, the target-substrate distance is of few cm; therefore, in the presence of an ambient gas, the vapour species in the plasma can collide several times with the gas molecules. Before their arrival on the substrate, the collisions can cause the nucleation and growth of the vapour plasma components in different sized particles. Therefore, particle dimension grows with the ambient gas pressure. On the contrary, by depositing in high vacuum condition, smaller particles are obtained and their distribution size is narrower [50].

Target fragmentation is more probable during the ablation of rough target surfaces, where the exposure of cracks and poorly attached particles to an intense laser beam causes the formation of crater edges, columnar structures, and deep voids. Any mechanical weakness can be easily dislodged. If these fragments are melted in the plasma, mainly owing to the interaction with the laser pulse, they will deposit as circularly shaped particles; otherwise, they will arrive on the growing film as irregularly shaped fragments [50]. Clearly, the presence of the debris is usually detrimental, since their adhesion on the substrate is poor and their shape is not controllable.

The ejection of liquid droplets occurs when the molten layer of the target is superheated, the metastable superheated liquid cannot sustain the tensile forces, vapour bubbles are created and grow in order to extract heat, and the explosive boiling (or phase explosion) of molten material from the target takes place [50].

In Figure 1, a typical schematic representation of a PLD set-up is shown. PLD is carried out in a vacuum chamber, where a nanosecond pulsed laser is focused on the target, which is continuously rotated in order to avoid piercing and to improve the morphology of the deposited film. Usually, the substrate is positioned in front of the target and a substrate heater can be present to allow the films to grow at a temperature higher than room temperature. A gas inlet is present when a gas buffer is used during the deposition experiments. Additional optical elements are used in order to characterize the ablation mechanism to study the laser-induced plasma expansion by emission spectroscopy or imaging techniques.

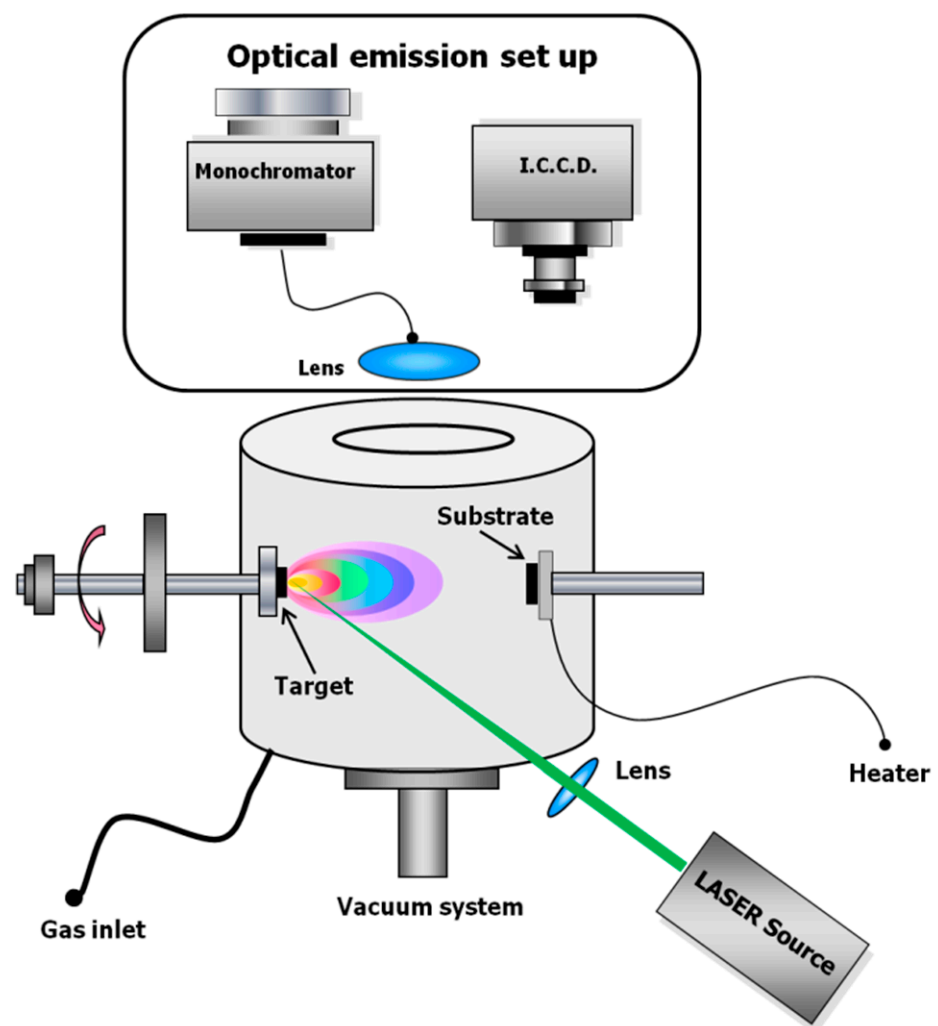


Figure 1. Experimental set-up for pulsed laser ablation and deposition.

3. PLD of Ion Doped HA Films

3.1. Nanosecond Ablation and Deposition of HA Films

In the early 1990s, the possibility to use PLD to deposit stoichiometric HA films was investigated. The first study was by Cotell et al. [51]. Since then, many authors have investigated the effects of temperature and pressure conditions on the crystalline phase and composition of the deposited calcium phosphate films. It was immediately known that films obtained by the ablation of the crystalline HA target with nanosecond UV laser sources in vacuum atmosphere are amorphous, irrespective of the substrate temperature. Under the same temperature conditions, the presence of a buffer gas allows to obtain crystalline calcium phosphate films, but it is possible to obtain crystalline HA films only in the presence of water pressure [52]. The versatility of the PLD technique was clearly highlighted, since by varying the pressure conditions and the gas reactivity, different calcium phosphate phases were deposited, with different biological behavior. Sing et al. [53] studied the ablation of HA in the 50–500 mbar range of water pressure and proposed that the buffer gas can aid the formation of crystalline films, reducing the kinetic energy of the ablated species and preventing the evaporation of the volatile phosphorous from the deposited film. The absence of water vapor gets to the formation of tetracalcium phosphate and/or TCP phases, instead of the hydrated HA, without any effect on the film stoichiometry. In fact, Arias et al. [54] observed that the water, present as vapor in the deposition chamber, ensures the OH^- groups incorporated in the apatite phase. Careful attention has to be paid to the choice of operative conditions since the CO_3^{2-} and HPO_4^{2-} groups replace the PO_4^{3-} groups at low and high pressure, respectively, resulting in films with worse crystallinity. Solla et al. [55] proposed that the use of RF during the deposition process could be beneficial for the film crystallinity, reducing the carbonate amount. Usually, film deposition is carried out in the presence of the oxidizing gas and the titanium substrate is heated at a temperature above 400 °C. Under these conditions, the HA film grows onto an oxidized titanium surface, whose presence decreases the adherence of the HA crystalline coating. To improve the mechanical properties of the bioactive coating, Nelea et al. [56] deposited a ceramic (TiN , ZrO_2 or Al_2O_3) buffer layer on the surface of the titanium alloy substrate to prevent the titanium diffusion onto the calcium phosphate deposit during post annealing treatments. It was widely reported that by operating at low fluence (in the 0.3–2 J/cm² range), the stoichiometric transfer of HA to the coating was not possible due to the decomposition or preferential ablation of some of its components. In fact, when the HA target is ablated at low fluence, its incongruent melting is possible with losing of the CO_3^{2-} groups and enrichment of the target surface with CaO species [57].

To deposit films with controlled crystallinity, composition, morphology, and stability under physiological conditions, it is essential to address the ablation mechanism and the effect of the experimental parameters on film growth. Since the early 1990s, laser-induced plasma obtained during HA ablation has been studied by CCD imaging and optical emission spectroscopy methods.

The mechanisms of nanosecond ablation and deposition of HA were first investigated by Baeri et al. [58]. They used a ruby laser ($\lambda = 694 \text{ nm}$) operating at fluence ranging from 0.01–1 J/cm² and observed that two different ablation mechanisms were effective, resulting in the peaked distribution of micron-sized particles above a more angularly dispersed film, whose origin could be the evaporation process. Their hypothesis was confirmed by Serra et al. [59], who studied the dynamics of the ablation of the HA target by an ArF laser ($\lambda = 193 \text{ nm}$, $\tau = 23 \text{ ns}$) in high vacuum ($5 \times 10^{-5} \text{ mbar}$) and in water pressure in the range of 0.01–1 mbar. They acquired the images of the laser-induced plasma by a fast intensified CCD and evaluated its front velocity of $2.3 \times 10^6 \text{ cm/s}$ for ablation in vacuum. Under this condition, the plasma was found to have a typical plume shape and a second slower emission was observed. The authors proposed that the second emission was due to the gas-phase segregation effect, whereas a lighter gas was present in the first plasma. The confinement effect of the background water gas modifies the form of the expanding plume, which assumes a spherical front with pressure of 0.1 mbar and an irregular shape

at 1 mbar. In this case, the irregularities disappear after about 20 μs when the plume stops assuming a spherical shape. The less-oriented shape of the emitted plasma in the presence of the ambient gas results in a more uniform coating thickness [60]. A third delayed emission of hot particles travelling at a velocity of 10^4 cm/s can be observed by using a higher wavelength nanosecond laser source (KrF, $\lambda = 248$ nm, $\tau = 30$ ns). This difference is reflected in the film morphology—HA films obtained by ArF ablation have a lower density of droplets with respect to films deposited by the KrF laser source [61]. Optical emission spectroscopy allows to recognize that faster emission is composed of atoms and ions: the CaI and CaII species are the most abundant with a predominance of CaII at fluence of 4.8 J/cm², whereas P and O are present as neutral. Molecular species (calcium oxides) are present in the second emission. Molecules are not directly released from the target, but probably synthesized in the first stage of the plasma expansion with the catalytic effect of the target surface [62,63]. Similar results were obtained by using lasers with different wavelengths. Agop et al. [64] studied the plasma emission of HA ablated by a Nd:YAG laser source ($\lambda = 532$ nm) and registered three components in the CCD images of the induced plasma. The electronic temperature, evaluated by the Boltzmann plot method build on the CaI and CaII emission lines, revealed the heterogeneity in the distribution of the internal energy of the plasma.

Considering the various experimental parameters that affect the ablation mechanism and, consequently, the physical chemical properties of the deposited films, Nishikawa et al. [65] studied the effect of the laser spot size on the Ca/P ratio, a factor that is critical to govern the calcium phosphate solubility in biological media. They observed that by increasing the size of the laser spot, coatings with Ca/P ratio similar to the theoretical Ca/P ratio for HA were obtained. Their results appear controversial, since they obtained positive or negative dependence of Ca/P with respect to the spot size, varying the pressure, temperature, and substrates used during the deposition experiments. Moreover, they evaluated the Ca/P ratio by XPS, a technique that is sensitive only to the first few nanometers of the coating. However, their study clearly demonstrates that the uniformity of the spatial energy distribution of the laser pulse is a factor that has to be considered to prepare stoichiometric HA films.

The effect of laser fluence on the properties of calcium phosphate coatings were investigated by Tri et al. [66], considering HA ablation with a KrF excimer laser and fluencies in the 2.4 – 29 J/cm² range. They observed that at higher fluence, it was possible to deposit crystalline HA films in vacuum and explain their results, considering that at these fluencies, the high pressure of the plasma can partially suppress P and H₂O evaporation, preserving the target composition. Moreover, at a high fluence, the ablated species have enough energy to migrate to the position with high bonding energy, leading to the formation of crystalline HA. Crystalline HA coatings were also obtained, depositing at room temperature and in vacuum with the Nd:YAG laser source ($\lambda = 532$ nm) at a fluence of 30 J/cm². With the use of low absorbance, the high fluence laser source gets to the expulsion of particulate with high kinetic energy and guarantees the formation of a crystalline, dense, and well-adherent coating at room temperature, opening the possibility to deposit on thermal-sensitive substrates [67]. Studying the first step of film growth by TEM microscopy, Checca et al. [68] investigated the effects of laser wavelength and fluence on the morphology and composition of HA films deposited with IR and visible nanosecond laser sources at high fluencies (in the 12.7 – 76 J/cm² range) and related these parameters with the ablation mechanism (Figure 2). They observed that the deposited films were formed by different structures, whose abundance and properties are dependent on the HA absorption at the laser wavelength. In particular, since green laser is less absorbed with respect to IR, during the ablation with green lasers, the explosion regime is more important, whereas with IR lasers, the coherent ion ablation prevails. Irrespective of the laser wavelength, they observed that CaP films were formed by an amorphous unstructured layer with nanoparticles grown over the films. This layer is denser and thicker when the IR source is used. Overlapping this layer, the authors observed spherical

particles, with the Ca/P ratio smaller than that of the target, ring-shaped particles with Ca/P ratio higher than that of the target, and large HA crystals. They considered that HA crystals are ejected from the target and ring-shaped structures are liquid droplets generated during the phase explosion regime, mainly with the green laser. Since phosphorus has a lower boiling temperature with respect to calcium, the droplets arrive on the substrate enriched with calcium. On the other hand, the observed spherical particles nucleate and grow in a dense gas phase enriched with phosphorus, as their composition confirms.

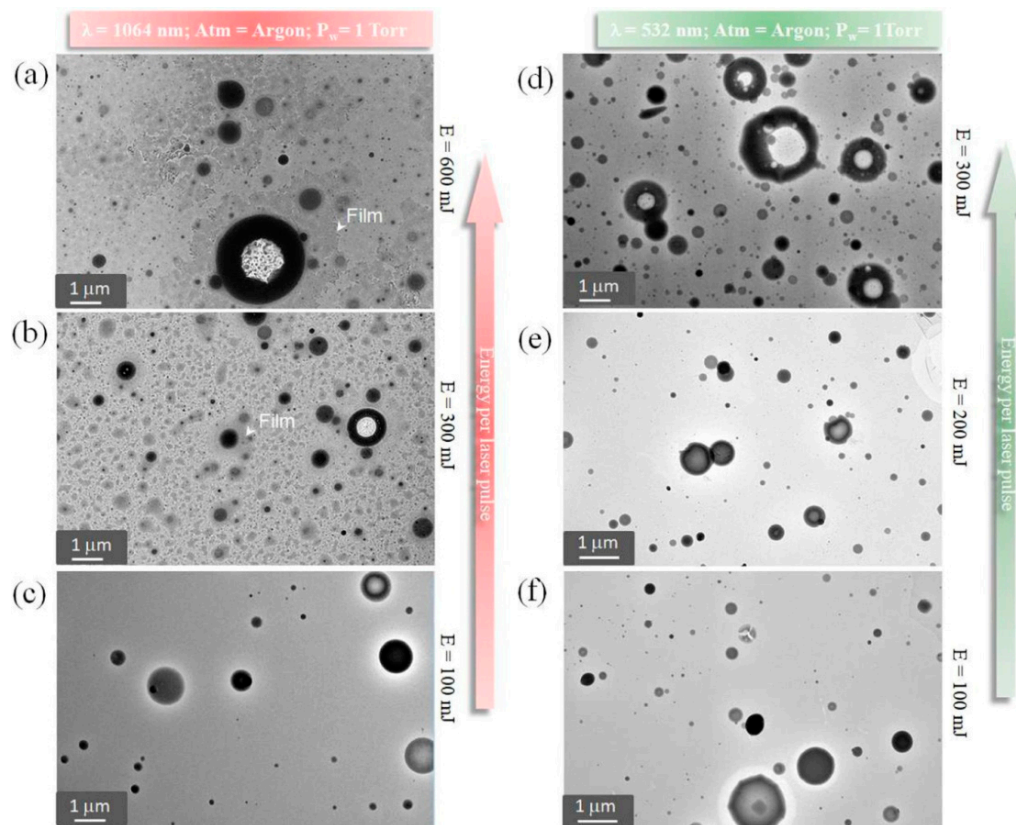


Figure 2. The effect of laser wavelength and fluence on the mechanism of HA ablation and film growth. (a–c) TEM images of HA films deposited at different fluencies by a ns laser source operating at 1064 nm; (d–f) TEM images of HA films deposited at different fluencies by a ns laser source operating at 532 nm. Reproduced with permission from [68], copyright from 2021 Elsevier.

In addition, the target properties, especially its density, determine morphology and composition of deposited films, were studied. Bao et al. [69] used HA target sintered at temperature ranging from RT to 1200 °C and observed that on increasing target density, the density of droplets on the films surface decreases. This effect has a role in film composition since droplets retain target stoichiometry, whereas films, mainly formed by gas condensation, suffer phosphorus depletion.

Guillot et al. [70] investigated the role of target optical absorptivity at the laser wavelength on the film morphology. They considered the ablation of pure HA and Mn-doped HA and observed that on increasing the target absorptivity, films with lower density of droplets were deposited. They related film morphology with the mechanism of laser ablation, observing that the plasma obtained by the ablation of the doped target had higher temperature and electronic density. The higher target optical absorption allows to produce a higher quantity of evaporated material, reflecting a smoother film morphology.

3.2. Substituted HA

Due to its structure, HA is able to host many metallic cations that can substitute Ca^{2+} ions, whereas anions such as F^- and CO_3^{2-} , can replace OH^- and PO_3^{4-} ions, respectively.

In particular, the presence of carbonated groups can be beneficial for HA solubility and bioactivity and many authors used carbonated HA as targets for PLD deposition [71]. Rau et al. [72] demonstrated that carbonated HA films are thermally stable and present improved nanohardness with respect to the target material. However, the partial phosphate substitution with carbonate is very frequent during laser deposition of calcium phosphate films due to the residual carbon dioxide present in the deposition environment or due to the exposition of the obtained films to atmosphere; we do not consider carbonate as a doping ion in our review.

- Mg

Magnesium is an essential element for living organisms; its deficiency causes the cessation of bone growth and generates bone fragility. Doping calcium phosphate materials with magnesium improves phosphate crystallization, modifying its dissolution rate in biological media [73]. Mróz et al. [74,75] studied the deposition of Mg-doped HA films obtained with an excimer laser source operating at $\lambda = 193$ nm and with a fluence of 7 J/cm^2 . The depositions were carried out in water pressure, the substrate temperature was set at 600°C , and $3 \mu\text{m}$ thick films were obtained. They demonstrated that 0.6% of Mg can be incorporated in an HA structure and by comparing the XRD spectra of Mg-doped deposits with undoped HA films obtained under the same experimental conditions, the effect of Mg on the crystallinity of coatings is clearly seen. The ability of the PLD technique to coat porous scaffolds was useful to deposit Mg HA films on 3D structured titanium-based implants that were tested in vivo in rabbit femurs [76]. Mg-doped calcium phosphate films were deposited at room temperature onto polymeric scaffolds [77], evidencing the higher activity of osteogenic differentiation markers with respect to both the uncoated scaffold and the undoped CaP-coated scaffold.

- F

In partially fluorinated apatite (FHA) and fluoroapatite (FA) F^- substitutes OH^- ions, modifying the HA crystal lattice in FA has higher symmetry. F^- substitution improves HA stability in body fluids, confers higher thermal stability, has a positive influence against osteoporosis, and promotes mineralization and crystallization of calcium phosphate during bone formation [78]. Ferro et al. [79] first studied the PLD deposition of FHA at room temperature with a Nd:YAG laser source operating at 532 nm and with a fluence of 12 J/cm^2 . The films obtained were mainly amorphous with the presence of the calcium phosphate ($\text{Ca}(\text{PO}_3)_2$) phase, The mean fluorine amount in the target was evaluated with 0.74 wt.% and target composition was well reproduced in films that had 0.54 wt % of fluorine, confirming the ability of the PLD technique to deposit films that retain the target stoichiometry [79]. The optimal conditions to obtain crystalline FHA films with KrF laser ($\lambda = 248$ nm) and with a pressure of 5×10^{-4} mbar of N_2 were studied by Rau et al. [80], varying in fluence and substrate temperature. They observed that films deposited at 2 J/cm^2 and $500\text{--}600^\circ\text{C}$ retain the target phase and composition. Irrespective of the laser source, fluence, and substrate temperature, FHA films show improved hardness with respect to the target materials. Fluorine-doped HA films ($\text{F} \leq 1\%$) were deposited with a 1024 nm laser source by Cao et al. [81]. They ablated a target obtained by mixing HA and CaF_2 and studied the bioactivity and biocompatibility of the as-deposited and annealed (500°C) films, comparing their behavior with undoped HA films obtained under the same experimental conditions. The beneficial effect of F doping on bioactivity was studied considering the formation of nanocrystalline HA during soaking in SBF solutions. Nanoflower and sponge-like HA structures were found on the FHA films, whereas the surface of the HA coatings did not see significant modifications in morphology after seven days of SBF soaking. The authors observed that fluorine was almost retained in FHA coating, confirming the positive role of the ion in the bone mineralization process. The cell compatibility of the coatings was tested in vitro, observing the proliferation of BMS cells. Hashimoto et al. [82] observed that FHA films deposited by a KrF laser and annealed at 450°C exhibit higher HMSC cell attachment,

compared with HA films deposited under the same conditions. Animal experiments and clinical studies to validate the material's performances *in vivo* have not been reported.

The combination of the beneficial effects of Mg and F substitutions in HA was investigated by depositing layered FHA and MgHA onto a titanium surface [83]. The Mg-doped layer gets to a high dissolution rate in the physiological medium and the lower F-doped layer provides for the hardness of the coating, resulting in a three-dimensional porous structure that could accelerate the apatite formation and induce cell proliferation.

- Sr

Strontium is present in the mineral phase of bones. It has been reported that *in vitro*, it increases the number of osteoblasts and reduces the activity of osteoclasts and *in vivo* it inhibits bone resorption and improves bone formation [84,85]. Strontium can replace calcium in the HA structure for the whole range of compositions, inducing a linear variation in the lattice constants. HA powder doped with different amounts of Sr was synthesized by the wet method and used to deposit thin films by nanosecond PLD using well-known deposition conditions operating at low fluence and with an excimer laser source by Cappuccini et al. [85]. The authors obtained films with a composition close to the target and with a homogeneous Sr distribution. The positive effect of Sr on osteoblast cell adhesion and activity was proved by comparing coatings with different Sr content. Pereiro et al. [86] deposited films by using a target obtained by mixing HA and $\text{Sr}(\text{CO}_3)_2$, showing that in the deposited films, Sr ions replace Ca^{2+} without any negative effect on the films' crystallinity. The biocompatibility of SrHA films was studied by De Bonis et al. [87] using dental pulp stem cells (DPSCs). Amorphous SrHA films were deposited at room temperature with a Nd:YAG laser source operating at a fluence of 12 J/cm^2 , where carbonate ions were accommodated in HA surface substituting hydroxyl and phosphate groups, as shown by XPS characterization. Increasing the deposition temperature, the crystallinity of the target was recovered, and films surface roughness and hardness increased, whereas the bioactivity and biocompatibility of the films were confirmed regardless of the deposition temperature.

- Si

Among the ions normally present in natural HA, Si plays a pivotal role in the early stage of mineralization and its deficit can be related to osteoporosis. It was demonstrated that Si increases osteoblast cells' activity, decreasing bone opposition to the artificial implants. PLD deposition of SiHA films with excimer laser and in water pressure was reported by Solla et al. [36,88]. They used targets prepared by mixing carbonated HA and a different source of silicon: synthetic SiO_2 , biological source of SiO_2 (diatomaceous earth) and silicon powder (in the range 2.5%–10%). Irrespective of the silicon source, the authors demonstrated that Si incorporation provokes diminution of the crystallinity of the films. The study of the composition of the films surface by XPS analysis allows to state that Si was present in the films as silicate groups, substituting the carbonate groups of HA instead of the phosphate ones [89]. They tested the adhesion and proliferation of osteoblast cells on the obtained SiHA films and proved the absence of toxicity of coatings obtained from targets with 7.5 at.% of Si. The presence of other minority ions improve the biological performances of Si-substituted HA [90]. Since it was reported that Si can be incorporated in HA lattice for amounts lower than 1.6% preserving its crystallinity, Rau et al. used targets with 1.4% of Si prepared by wet synthesis [91]. They obtained crystalline films deposition at $600 \text{ }^\circ\text{C}$, at low fluence (2 J/cm^2), and at pressure of $5 \times 10^{-2} \text{ Pa}$ of N_2 ; however, due to the incongruent melting of HA, the formation of the CaO phase occurs and films present higher Ca/P ratio than the target. In a successive study, the same authors investigated the mechanical properties of SiHA films deposited by heating the substrate at a temperature of $400\text{--}750 \text{ }^\circ\text{C}$. They observed the improving of the microhardness of the coating with the increasing of the deposition temperature, but at higher temperatures, the formation of CaTiO_3 phase take place. The authors concluded that the optimal temperature range to deposit SiHA films is $400\text{--}600 \text{ }^\circ\text{C}$, with the possibility to obtain coatings with tunable

surface roughness and mechanical properties. The bioactivity ability of SiHA was proved by soaking the films deposited onto titanium substrates in α -MEM solution [92].

The combination of the beneficial effects of Sr and silicate substitutions in HA was investigated by depositing films with different Sr/Si content [93]. The deposited films, with the usual globular morphology and accurate preservation of the targets composition, allow the healthy proliferation of hBMS cells.

- Ag

Silver exhibits strong toxicity with respect to a wide range of micro-organisms and the antibacterial activity of silver doped materials is related to the amount of Ag^+ ions released. Its antibacterial activity makes Ag a relevant element to improve the properties of HA coatings, supporting the inhibition of bacterial colonization on the surface of implants, and imparting strength and toughness to the coatings [94]. Considering AgHA films deposited by PLD with an excimer laser, no difference in antibacterial activity of amorphous and crystalline coatings was observed [95]. Antibacterial activity close to 100% with respect to *Escherichia coli* bacteria was reported for films with 1.2% of Ag obtained with the ablation of metallic Ag and HA targets, alternatively. AgHA target prepared by the sol-gel method was used for PLD deposition by Sygnatowicz et al. [96]. The target has a multiphase composition with silver cluster of about 100 nm, but only the HA phase was observed in films annealed at 600 °C. Amorphous and crystalline films have different stability in solution, as expected. Recently the use of magnesium alloys as implants was proposed. In fact, these biodegradable materials dissolve in vivo during the healing process and do not require additional surgery. Silver coating or doping of magnesium implants is not a suitable strategy since Ag and Mg will form a galvanic pair with high corrosion rate in biological media. The laser deposition of TCP doped with different amount of Ag was proposed by Kotoka et al. [97] to protect biodegradable implants from corrosion in biological media, preserving the well-known antibacterial activity of Ag. They proved that corrosion resistance increases with a rise in the amount of dopant up to 5%—with higher Ag content, corrosion resistance decreases.

- Mn

Mn^{2+} increases the ligand binding affinity of integrin and activates cell adhesion. The first study that reported the deposition of Mn-doped HA films is by Gyorgy et al. [71]. Depositing with an excimer laser in O_2 pressure on Ti substrates, they obtained films with a granular morphology. TEM cross-section images of the grown films show a granular and compact structure [98]. The films present improved fibroblast (L929) and osteoblast (hFOB1.19) cell response with respect to the Ti's bare surface, suggesting that MnHA films on metallic Ti implants should provoke a faster integration with the bone tissues. It is known that crystalline HA has lower bioactivity and lower ALP activity with respect to low crystalline calcium phosphate materials. Bigi et al. [99] demonstrated that the beneficial effect of Mn ions for promoting and triggering cell proliferation can counterbalance the effect of HA crystallinity. With PLD, the authors were able to deposit crystalline Mn-doped HA films with good mechanical and biological properties.

- Fe

Among the various vicarious elements, Fe is one of the most interesting, due to its no-cytotoxicity to osteoblast and intrinsic magnetic properties, which allow to produce biomedical materials suitable for magnetic stimulation in situ. Rau et al. [37] deposited Fe–HA crystalline films by PLD with a Nd:YAG laser source operating at 532 nm in vacuum atmosphere with high fluence and at a substrate temperature of 600 °C. The films had good mechanical properties in terms of nanohardness and a typical morphology of nanosecond deposited coatings, characterized by a compact and irregular structure. The magnetic properties of PLD-deposited Fe–HA films were studied by Curcio et al. [100]. In their study, the authors prepared Fe-based nanoparticles by laser ablation of a metallic Fe target in water. The obtained nanoparticles were mixed with HA powder to prepare targets used

for PLD experiments. Films deposited at 500 °C were composed of HA and magnetite phases, irrespective of the oxidation state of the used Fe nanoparticles due to the oxidizing effect of laser-induced plasma during the ablation experiment. The iron oxidization was advantageous since magnetite is the preferred one among iron oxides for biomedical applications, thanks to its higher magnetization and susceptibility and the absence of cytotoxic effects. The superparamagnetic behavior of the deposited films was tested.

Fe-doped OCP was deposited on biodegradable Mg–Ca alloys by Antoniac et al. [101]. The authors demonstrated that iron doping improves the corrosion resistance of the alloy with respect to undoped OCP coatings, probably due to the modified structure and morphology of the doped coating (Figure 3).

- Other elements

There are many studies considering the laser deposition of doped HA with elements that give functional properties to the coatings. PLD is a very affordable technique, since it allows the stoichiometric transfer of target composition to the films. Among the doping elements, the incorporation of selenium in HA coatings was exploited by Rodriguez-Valencia et al. [38]. In a pioneering study, the authors mixed HA and Se powder at different ratios and verified that Se is present in the HA lattice as SeO_3^{2-} displacing CO_3^{2-} groups. They varied the Se amount in the coating with a fine control by varying the target composition. Coatings obtained with the lower Se percentage (0.6%) showed the absence of cytotoxicity on pre-osteoclastic MC3T3-E1 cells and evidenced their effectiveness to inhibit bacterial growth (*P. aeruginosa* and *S. aureus*), but the Se activity as antioxidant in the cells was not proved. The targets obtained by mixing HA with copper oxide and zinc oxide, respectively, were used by Hidalgo-Robatto et al. [102] to deposit films with antibacterial activity. They demonstrated that both Cu and Zn can be incorporate into the HA lattice, substituting Ca^{2+} and inducing a deformation of the crystal that is more important when the doping ion is Cu. The possibility that doping ions are present in interstices of the network was not excluded.

Ahmed et al. [103] deposited AuCHA films on the surface of porous alumina scaffold. They observed an increase in surface roughness (evaluated by AFM measurements) with rise in Au amount and suggested that this effect could be related to the lower crystallinity of the target with the higher dopant amount. The increased surface roughness is beneficial for the biocompatibility of the coatings with HFB4 cells that proliferate through the coated scaffold as a function of Au amount.

Metal oxides can be added to HA with the aim to improve its mechanical properties. Gyorgy et al. [104] observed that films of HA doped with ZrO_2 exhibit lower crystallinity with respect to undoped HA films deposited by PLD under the same experimental conditions (laser source, fluence, and water pressure). However, ZrO_2 seems to have a negative effect on the coating biocompatibility; in fact, the number of Hek293 cells' adherence was lower for the doped HA with respect to the undoped.

The reviewed literature reporting PLD of ion-doped HA is given in Table 2.

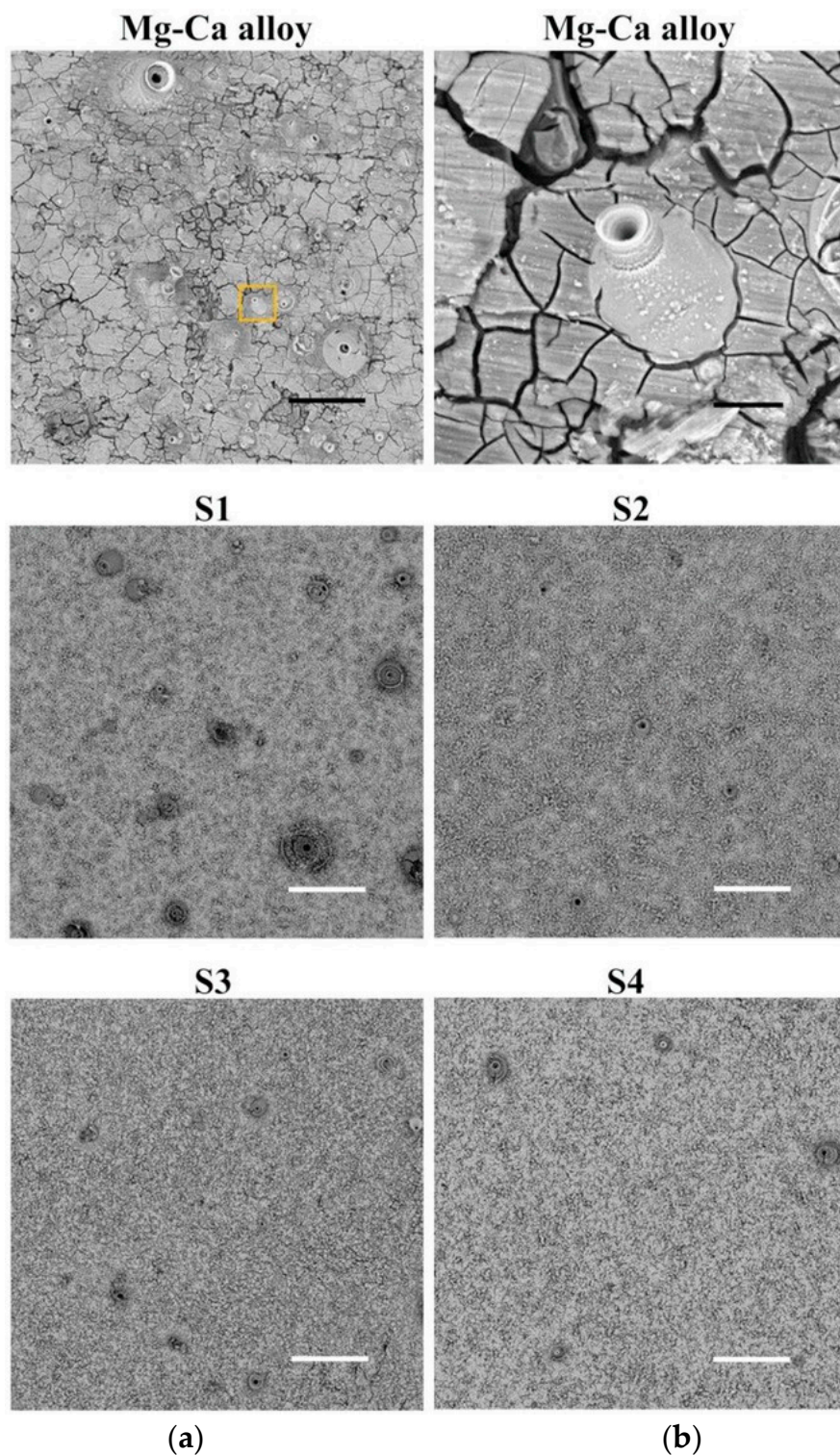


Figure 3. SEM images of coated and uncoated Mg–Ca alloys after the electrochemical tests: Mg–Ca alloy (a) 100 μm , crater-like formation on Mg–Ca alloy (b) 10 μm . TCP coated Mg–Ca: S1 ($T_{\text{substrate}} = \text{RT}$; $N_{\text{pulse}} = 12.000$), S2 ($T_{\text{substrate}} = 300\text{ }^{\circ}\text{C}$; $N_{\text{pulse}} = 12.000$), Fe-TCP coated Mg–Ca S3 ($T_{\text{substrate}} = \text{RT}$; $N_{\text{pulse}} = 6.000$) and S4 ($T_{\text{substrate}} = 300\text{ }^{\circ}\text{C}$; $N_{\text{pulse}} = 6.000$). All films were deposited with a ns laser source operating at $\lambda = 355\text{ nm}$, $\phi = 2\text{ J}\cdot\text{cm}^{-2}$, $d = 4\text{ cm}$. In S1, S2, S3 and S4 images the scale bar is 100 μm . Reproduced with permission from [101], copyright from 2020 WILEY-VCH Verlag GmbH & Co. KGaA, Weinheim.

Table 2. Pulsed laser deposition (PLD) experimental details and properties of films of substituted HA.

Doping Element (s)	Laser Source	Deposition Conditions	Substrate	Properties	Ref.
Mg	193 nm, 20 ns, 50 Hz	7 J/cm ² , 600 °C, 35 Pa air pressure	Ti6Al4V	Improved crystallinity	[74]
	193 nm, 20 ns	7 J/cm ² , 450 °C, 30 Pa water pressure	Ti6Al4V	Osteogenic differentiation	[75]
	193 nm, 20 ns, 50 Hz	2 J/cm ² , RT, 3.2 × 10 ⁻² mbar water pressure	PLC scaffold	Osteogenic differentiation	[77]
F	532 nm, 10 ns, 10 Hz	12 J/cm ² , RT, 1 × 10 ⁻⁴ Pa	Ti	Hardness	[79]
	284 nm, 17 ns, 5 Hz	2–7 J/cm ² , 400–600 °C, 5 × 10 ⁻⁴ mbar N ₂	Ti	Polycrystalline films with improved mechanical properties	[80]
	248 nm, 20 ns, 10 Hz	1 J/cm ² , RT, 1 Pa water pressure, post annealing	Ti	Dissolution resistance, HMS cells adhesion	[82]
	1024 nm, 18 ns	Post annealing	Ti	In vitro bioactivity, BMS cells adhesion	[81]
Sr	248 nm, 7 ns	2 J/cm ² , 400 °C, 50 Pa water pressure	Ti	Osteoblast cells adhesion and activity	[85]
	193 nm, 10 Hz	3.2 J/cm ² , 460 °C, 45 Pa water pressure	Ti, Si	Incorporation of Sr in the HA lattice	[86]
	532 nm, 7 ns, 10 Hz	12 J/cm ² , Rt-500 °C, 1 × 10 ⁻⁴ Pa	Ti	DPS cells adhesion	[87]
Si	193 nm, 10 Hz	460 °C, 0.45 mbar water pressure	Ti, Si	Diminution of films crystallinity with increasing of Si content	[36,88]
	193 nm, 10 Hz	460 °C, 0.45 mbar water pressure	Ti	Adhesion and proliferation of osteoblast cells	[90]
	248 nm, 17 ns, 5 Hz	2 J/cm ² , 600 °C, 5 × 10 ⁻² mbar N ₂	Ti	In vitro bioactivity	[91,92]
Ag	248 nm, 20 ns, 10 Hz	2 J/cm ² , RT-600 °C, 40 Pa water pressure	Ti, fused silica, Si	Antibacterial activity	[95]
	248 nm, 25 ns, 10 Hz	2–3 J/cm ² , 300 °C, 10 ⁻⁶ mbar, post annealing	Al	Amorphous and crystalline films with antibacterial activity	[96]
	248 nm, 25 ns, 10 Hz	4.5 J/cm ² , 500 °C, 50 Pa water pressure	Ti, TiO ₂ nanotubes	Antifungal activity	[105]
	248 nm, 20 ns, 10 Hz	2 J/cm ² , RT, 5 × 10 ⁻⁶ Torr	Mg	Corrosion resistance	[97]
Mn	248 nm, 20 ns, 2 Hz	2 J/cm ² , 300–400 °C, 10 Pa O ₂	Ti	Osteoblast proliferation	[71]
	248 nm, 30 ns, 2 Hz	400 °C, 10 Pa O ₂	Ti	Osteoblast differentiation on crystalline CHA	[99]
Fe	532 nm, 10 ns, 10 Hz	90 J/cm ² , RT-600 °C, 4 × 10 ⁻⁴ Pa	Ti	Crystalline films with improved hardness	[37]
	532 nm, 10 ns, 10 Hz	37 J/cm ² , RT-500 °C, 4 × 10 ⁻⁴ Pa	Ti	Magnetic properties	[100]
	355 nm, 7 ns, 10 Hz	2 J/cm ² , RT-300 °C,	Mg-Ca alloy	Corrosion resistance, reduction of degradation rate	[101]
Se	193 nm, 10 Hz	3.2 J/cm ² , 460 °C, 45 Pa water pressure	Ti, Si	Antibacterial activity	[38]
Cu, Zn	193 nm, 10 Hz	3.2 J/cm ² , 460 °C, 0.45 mbar	Ti6Al4V	Osteoblast cells growth and proliferation, antibacterial activity	[102]
Au	1064 nm, 8 ns, 10 Hz	4.5 × 10 ⁻⁴ Pa	Alumina scaffold	HFB4 cells adhesion and proliferation	[103]

4. PLD of Glass and Glass-Ceramic Coatings

The first attempt to obtain bioactive glass films by PLD was made by D'Alessio et al. [106] in the late 1990s. They used a visible laser source to deposit commercial 45S5 Bioglass® on Ti4Al alloy. In particular, they studied the effect of laser fluence on ablation and deposition rates. The fluence had to be high enough to induce the material ablation, but not so high to induce particle ejection by target fragmentation. In this case, depositions were carried out by using the second harmonic of Nd:YAG laser ($\lambda = 532$ nm) at room temperature and vacuum atmosphere and varying laser fluence in the range 0.5–14 J/cm². They found a high ablation threshold of 3.5 J/cm², due to the transparency of such material to the visible wavelength; therefore, for a significant ablation rate, a minimum fluence value of 7.5 J/cm² is necessary. By evaluating the dependency of the deposition rate on the laser fluence, they observed a growing linear trend starting from 9 J/cm². They studied the effect of the laser fluence by analysing the plasma plume by optical emission spectroscopy and laser ablation inductively coupled plasma mass spectrometry (LA-ICP-MS) [107]. The vapour phase was

demonstrated to have a different composition from that of the target material; in particular, Si and P% were lower than that of the expected values. Similar results were obtained by applying LA-ICP-MS. Therefore, the ablation was not congruent by using a ns-pulsed laser in the fluence range from 3.5 (threshold value) to 14 J/cm². Moreover, by performing SEM-EDX analysis, they could observe the films' morphology and composition. All the films, irrespective of the laser fluence, were characterized by a large number of micrometric droplets, which preserve target composition, embedded in a uniform matrix with a different composition (i.e., lower amount of Si and P). However, by analysing larger areas of the films, they found that the average composition was close to the target one, indicating that the droplets are the main component of the film. The presence of micrometric droplets is not a drawback in the case of BG coatings for bone tissue application. Moreover, no effect of the laser fluence were found on film adhesion and composition. The effect of laser fluence was investigated also by Serra et al. [15], who deposited a bioactive glass target (42% SiO₂, 20% Na₂O, 10% K₂O, 20% CaO, 3% P₂O₅, 5% MgO) by an ArF excimer laser beam ($\lambda = 193$ nm) varying the laser fluence from 0.2 to 6.0 J/cm². They demonstrated the linear dependence of the deposition rate on the laser fluence, in accordance with results obtained by D'Alessio et al. [106]. Despite the similarity of the ablated target, Serra et al. found a threshold value was of 0.2 J/cm², sensibly lower than the value reported by D'Alessio et al.; this is mainly due to the different laser wavelength since glass absorbs UV radiation stronger than visible ones. Moreover, Serra et al. investigated the effect of the laser fluence on the characteristics of the films, finding significant difference on film roughness but no differences in mechanical properties. In addition, Sanz et al. [108] evidenced the effect of the laser fluence on film morphology and roughness. They used the third harmonic of a Nd:YAG laser ($\lambda = 355$ nm) at two different laser energy (i.e., 50 and 100 mJ) for depositing in vacuum a niobo-phosphate bioactive glass (NbP-BG). By SEM and AFM analysis of films deposited at the two different conditions (Figure 4), they evidenced a greater amount of larger droplets on the films obtained at higher laser energy, resulting in higher roughness values. They attributed the presence of droplets to a splashing mechanism observed during the ablation process, which usually increases with the rise in laser energy. Floroianet al. [109] investigated the effect of the fluence of a KrF excimer laser source ($\lambda = 248$ nm) on the deposition of two different glasses with two different silicate content (6P57 and 6P61, with 57 and 61 wt.% of silicate, respectively). They deposited in low pressure oxygen atmosphere varying laser fluence between 4 and 8 J/cm², finding that values of 5.5–6 J/cm² allowed to preserve target stoichiometry and obtain a smooth film.

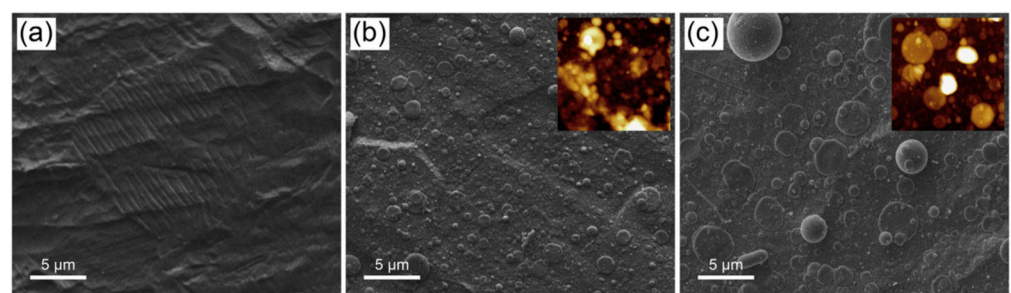


Figure 4. Effect of laser fluence on BG film growth: (a) Ti surface, BG deposited on Ti at (b) 50 mJ and (c) 100 mJ. Reproduced with permission from [108], copyright from 2019 Elsevier.

Deposition atmosphere is also an important parameter affecting both film composition and crystallinity. It is well known that PLD can be carried out on vacuum or in a reactive or unreactive gas atmosphere. Several studies have demonstrated that during ns-PLD, target stoichiometry is nearly congruently transferred to the films.

In particular, by depositing bioactive glass or glass-ceramic in vacuum condition, target stoichiometry is preserved for droplets or particles ejected directly from the target, while portions that originated from the condensation of the gaseous phase show small losses of lighter and more volatile species during plasma expansion [106–108,110–112].

Moreover, some researchers have observed that bioactive glass coatings deposited in vacuum are characterized by a different bonding configuration with respect to the target, even if composition is retained [15,110,113]. In particular, by depositing silicate glass by the means of a ArF excimer laser ($\lambda = 193$ nm) at 200 °C in vacuum, they observed that by the FTIR spectroscopic technique, a decrease in the Si–O–NBO/Si–O–Si ratio was responsible for the bioactive behaviour of the coatings. On the other hand, Kwiatkowska et al. [114] observed the opposite effect on the bonding configuration of a glass with similar composition deposited in vacuum with a Nd:YAG laser ($\lambda = 1064$ nm) at room temperature, supposing higher bioactivity for the films rather than the bulk form. In order to study the effect of gaseous atmosphere on bonding configuration, deposition in different gas environments were carried out. González et al. [115] obtained films with different compositions and bonding configurations by depositing the same target materials in vacuum (10^{-4} mbar) and in N₂O (0.05 mbar) with a ArF excimer laser ($\lambda = 193$ nm); in particular, they obtained a more oxidised film in an N₂O atmosphere, as detected by EDS. This oxygen enrichment induces a decrease in Si–O–NBO/Si–O–Si ratio due to the saturation of Si–O–NBO groups, reducing the effect of network modifiers cations (i.e., Na⁺, Ca²⁺).

Listeet al. [116] deposited in H₂O, NH₃, N₂O, and Ar. First of all, they deposited at different Ar pressures (from vacuum 10^{-3} to 1 mbar), observing an exponential decreasing of the film growth with the increasing of Ar pressure, due to the influence of the gas on the velocity of the ablated species during the plasma expansion. In addition, they noted the decrease of the Si–O–NBO/Si–O–Si ratio with the increase in pressure. Furthermore, in N₂O or H₂O (oxidizing) atmospheres, Si–O–NBO content is reduced; in fact, UV laser radiation ($\lambda = 193$ nm) promotes the dissociation of N₂O or H₂O and leads to the formation of oxygen radicals, promoting the saturation of Si–O–NBO. They, therefore, stated that bioactive glass films should be deposited in vacuum or at very low Ar pressure in order to obtain a good Si–O–NBO/Si–O–Si ratio (~1). They further tested the presence of a small amount of ammonia in the deposition chamber (0.05 mbar), observing a beneficial effect of the reducing atmosphere on the Si–O–NBO/Si–O–Si ratio. Subsequently, Borrajo et al. [113] studied the effect of the influence of Si₂H₆/Ar and NH₃/Ar at growing pressure on the properties of bioactive silicate glass film deposited with an ArF laser. They demonstrated that the presence of disilane inhibits the formation of Si–NBO groups while ammonia at low pressure favors their formation, similarly to the vacuum condition. The same authors [117] concluded that vacuum is the most appropriate condition for depositing bioactive glasses. In addition, Zhao et al. [118] studied the role of pressure on bioactive glass (45S5), depositing with a ArF excimer laser ($\lambda = 248$ nm) at 200 °C at different Ar pressure (0–60 Pa), producing findings similar to that reported in [116]: all the coatings are characterized by a lower Si–O–NBO/Si–O–Si ratio with respect to the target and with increase in Ar pressure, this ratio decreases. However, Zhao et al. [118] observed a linear decrease of the deposition rate with increase of the Ar pressure. In addition, they explained the origin of the different kinds of particulates present in the deposited film; in accordance with D'Alessio et al. [106], they attributed the presence of round-shaped bigger particles to liquid droplets expelled by a super-heated target surface, while smaller nanometric particles originated from the condensation of the vapour phase, whereas irregularly shaped particles were due to the target fragmentation.

Several studies demonstrated that by depositing in vacuum or at very low pressure of unreactive gas, it is possible to preserve the Si–O–NBO/Si–O–Si ratio of the target [113,115–118], whereas the use of an oxidant gas (such as N₂O) promotes the reduction of Si–O–NBO groups and the adsorption of water [115,116]. The best pressure conditions to deposit bioactive glass ceramic films by PLD were not uniquely definite; in fact, many studies reported deposition in oxygen atmosphere, showing the good bioactivity and biocompatibility of the deposited films [104,109,119–141].

Several studies have been devoted to the effect of deposition temperature on films' characteristics, both in terms of physical and chemical properties: since the mobility of the ablated species on the substrate is strongly dependent on the deposition temperature, this

parameter has a great incidence on the film morphology and crystallinity. Serra et al. [15] varied deposition temperature in the range of 25–500 °C, at constant pressure and fluence, in order to investigate the change in bonding configuration due to network rearrangement during the film deposition. They found a slight increase in the Si–O–NBO/Si–O–Si ratio for the film deposited at 200 °C. Gyorgy et al. [104], while depositing bioactive glass with KrF excimer laser at a substrate temperature in the range 400–500 °C, observed no difference in XRD pattern of the obtained films, which were all poorly crystalline. Zhao et al. [142] investigated the effect of deposition temperature on both crystallinity and bonding configuration on bioglass coatings deposited with ArF laser at 20, 200, and 500 °C. All the registered XRD spectra are typical of a vitreous material, while from FTIR spectra, it was possible to detect different bonding configurations. In particular, they observed an increase in Si–O–NBO/Si–O–Si ratio with the substrate temperature. They attributed this phenomenon to the deposition mechanism: since species inside the plasma rapidly condense and cool on the substrate surface, it is possible to observe the segregation of cations (modifiers), originally well dispersed in the silicate network of the target material. This segregation causes inhomogeneity of film composition and the formation of a major number of Si–O–Si groups. However, ablated species can retain a certain degree of kinetic energy and diffuse on the substrate surface, when heated. In addition, the authors studied the effect of substrate temperature also on the adhesive strength of deposited films. By heating the Ti6Al4V substrate at 200 °C, the best balance between bonding configuration preservation and adhesive strength was achieved. Rau et al. [111] investigated the effect of substrate temperature on crystallinity and roughness of a glass-ceramic material, named RKKP, deposited by Nd:YAG laser ($\lambda = 532$ nm) in vacuum at 100, 300, and 500 °C. Only the film deposited at 500 °C showed contributions in the EDXRD (energy dispersive X-ray diffraction) pattern, attributable to a number of crystalline phases. As regard films roughness, unexpectedly, the authors noticed a smoothing of coating surfaces with increase in temperature. The same research group [143] carried out a similar study on another glass-ceramic material; they performed PLD at 25, 300, and 600 °C, obtaining a crystallized film only at 600 °C. Moreover, a Cu-containing BG deposited in similar conditions also showed a crystalline structure in the XRD pattern when deposited at 500 °C [144]. Deposition temperature is a key parameter when the glass and glass-ceramic materials tend to crystallize. It is well-known that bioactive glass usually shows mechanical performances not appropriate for load-bearing applications; therefore, the presence of crystalline phases in the vitreous matrix is a way to improve mechanical properties [145]. However, this causes a worsening of the bioactivity properties, as demonstrated by Curcio et al. [146]. In this case, the authors deposited Mn-containing RKKP at room temperature and 500 °C, obtaining amorphous and crystalline films, respectively. They studied the *in vitro* bioactivity following the standard Kokubo soaking test simulated body fluid (SBF) [147]. The film dissolution and comparison of the typical hydroxyapatite cauliflower structure was found to be slower for the crystalline film deposited at 500 °C, as evidenced by SEM images (Figure 5).

Curcio et al. [148] deposited carbon/RKKP composite films at different substrate temperatures (i.e., room temperature, 300, and 500 °C) with the aim to obtain amorphous thin films with enhanced hardness. They demonstrated the improvement in film hardness with the increase in deposition temperature, together with the absence of crystalline phases (even depositing at 500 °C), thanks to the presence of a carbonaceous network well dispersed in the coatings. In addition, they analysed the effect of the substrate temperature on the films' morphology and roughness by SEM and AFM technique. As visible in Figure 6, all the films are characterized by micrometric particles embedded in a compact matrix of nanometric particles. With the increase in substrate temperature, film densification, due to the aggregation and coalescence of nanoparticles, is seen, which increases the surface roughness value.

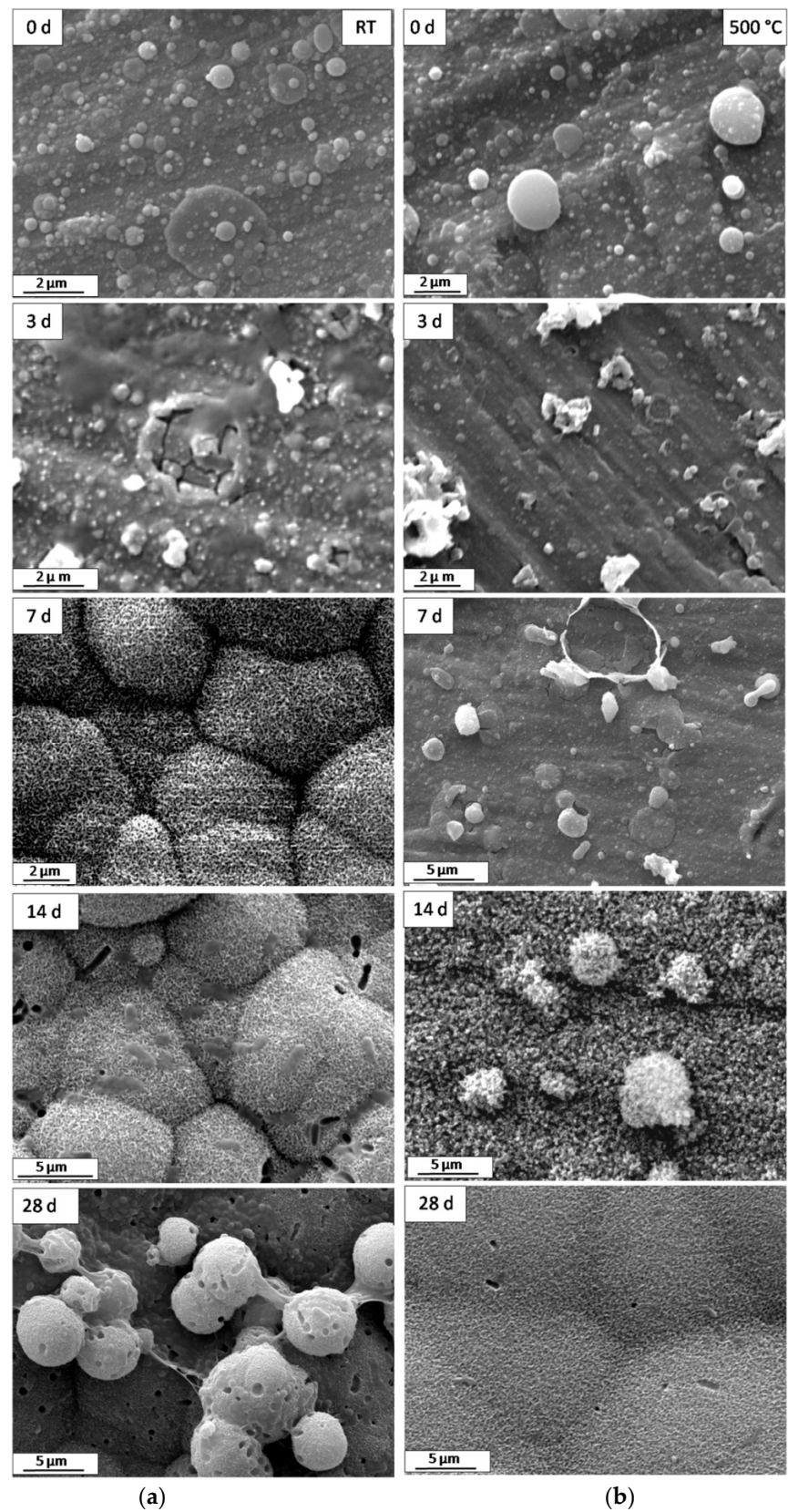


Figure 5. Effect of film crystallinity on in vitro bioactivity: SEM images collected upon RKKP-Mn films deposited at RT (a) and 500 °C (b) after different immersion time points in SBF. Reproduced with permission from [146], copyright from 2018 Elsevier.

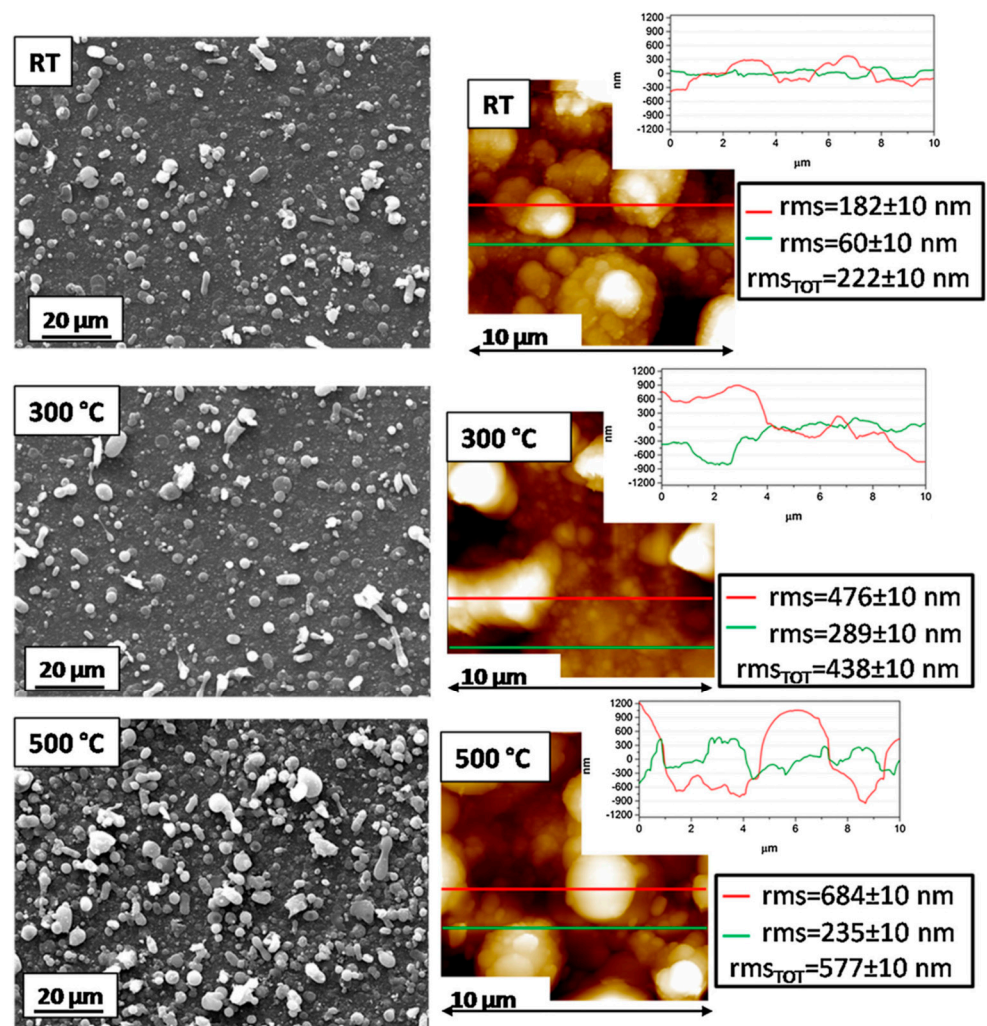


Figure 6. Effect of deposition temperature on BGC film growth. Reproduced with permission from [148], copyright from 2017 Springer.

As regards substrate materials, metals, and more specifically stainless steel (SS), Ti and its alloys are the most used for hard-tissue implants, thanks to their high tensile and yield strength and resistance to fatigue, creep, and corrosion. Therefore, most of the BG and BGC were deposited on the metal substrate with the aim to obtain a suitable coating for load-bearing implants [104,111,112,125,127,132,140–142,148–155]. Some of them are preferred to modify the Ti surface by chemical etching [108,114,129] in order to change the surface roughness [156], while Ma et al. [157] processed Ti alloy by micro-arc oxidation, with the aim to obtain a rough and porous oxide surface layer. González et al. [158] proposed a new type of substrate based on biomorphic silicon carbide ceramics with improved mechanical and bioactivity properties as an alternative to Ti implants. SiC was obtained by molten-Si infiltration of carbon templates produced by controlled pyrolysis of wood pieces. The obtained biomorphic SiC is characterized by porosity and mechanical features similar to that of bone tissue. They tested different types of wood and BG with different compositions [159–161], obtaining promising results for the application of these systems in hard-tissue related implants. Another revolutionary route for improving implants osteointegration is the production of bioresorbable implants, generally made in Mg and its alloys, which are supposed to be completely degraded after the bone healing [162]. However, the degradation rate of magnesium and its alloys is too rapid to match the kinetics of bone healing; in addition, it is possible that corrosion mechanisms occur. To overcome these problems, coatings with a biodegradable film, able to delay the degradation

of the implant, could an appropriate solution [163]. Only two research groups [124,164] have studied the possibility to cover this kind of bioresorbable substrate with BG or BGC by using PLD. In particular, Mihailescu et al. [124] carried out only a standard physico-chemical characterization of the obtained BG-coated Mg substrate, while Rau et al. [164] deposited RKKP BGC on a Mg–Ca substrate (1.4 wt.%) and examined corrosion resistance of the uncoated and coated Mg–Ca alloys in simulated body fluid (SBF). RKKP-coated Mg–Ca showed a higher electropositive corrosion potential value (−1.68 V) and a corrosion current density 10 times smaller than the uncoated Mg–Ca, providing a suitable corrosion behaviour for possible use as degradable implants.

Some research groups have investigated the use of BG and BGC coatings on polymeric substrates for both hard-tissue regeneration and wound-healing applications [120–123,133,135,137]. Wu et al. [133], by depositing akermanite (AKT) on polylactic acid (PDLLA) and polysulfone (PSU) films (obtained by casting), obtained systems for bone regeneration and replacement with improved surface roughness, hardness, bioactivity, and osteogenic and angiogenic activity. The same research group deposited AKT [120] and a Cu-containing bioactive silicate glass-ceramics [121] on artificial ligament for anterior cruciate ligament (ACL) reconstruction made in polyethylene terephthalate (PET) fibers. By performing an *in vivo* test, they demonstrated that PLD of bioactive glass on ACL is a promising way to overcome problems related to PET, such as low wettability and bioactivity, which causes a weak mechanical anchorage in the bone tunnel after implantation. Duta et al. [137] demonstrated the *in vitro* bioactivity of ultra-high molecular weight polyethylene acetabular cups (UHMWP) covered by BG films. Chen et al. [135] used a barrier collagen membrane as a substrate for the deposition of $\text{Ca}_2\text{ZnSi}_2\text{O}_7$ bioactive glass. The aim was the upgrade of this membrane from a simple physical barrier to a bioactive barrier with multiple effects on bone repair. In this way, they proved, by *in vitro* and *in vivo* tests, the possibility to produce new generation collagen membranes with osteoimmunomodulatory and osteogenic properties.

The possibility to coat proper substrates with BG and BGC thin films for wound-healing applications has been exploited by a few research groups [122,123,134]. They combined the physical guide of a patterned electrospun membrane with the angiogenic properties of BG. For this purpose, they [123,134] deposited two different BGCs on a PDLLA/PCL membrane for skin wound healing applications, especially helpful for diabetic patients with a chronic hyperglycemic state, which prevents correct blood flow, causing a lack of angiogenesis and slow wound healing. Moreover, to further improve the angiogenic activity and impart antibacterial properties to a glass/polymer system for wound healing application, Li et al. [122] incorporated copper in the BG composition. They used as substrate a natural collagen membrane, in particular, the egg shell membrane, which naturally owns antibacterial properties.

Several studies concerning the PLD of bioactive glass and glass-ceramic have been conducted up to now; and mechanical properties, biocompatibility, and bioactivity (both *in vitro* and *in vivo*) have been demonstrated, as shown in Table 3.

As regard mechanical properties, the excellent adhesion of 45S5 films deposited at room temperature on Ti alloy was demonstrated by the scratch test, showing that the deformation of a substrate was easier than the film detachment [107]. By increasing substrate temperature, adhesion properties may be enhanced, thanks to the reduction in thermal stress at the film-substrate interfaces; however, in the case of Ti and Ti alloy substrates, it is possible to observe opposite trends at temperatures up to 120 °C due to the easy formation of TiO_2 on the substrate surface, which is highly brittle and leads to the reduction of adhesion strength at the interface [142]. On the other hand, the increase in substrate temperature allows to improve films hardness not only because high temperature induces the formation of crystalline phases but also due to the film densification [111,149]. Many authors have demonstrated *in vitro* bioactivity by performing the Kokubo soaking test in simulated body fluid (SBF) solution [147,165] and several types of cells were incubated in contact with BG or BGC coatings, demonstrating not only their good biocompatibility, but

also the capacity to induce osteogenic and/or angiogenic differentiation on mesenchymal or stromal stem cells. A few research works have shown the osteointegration of implants coated with BG or BGC by in vivo tests.

All these studies, listed in Table 3, have demonstrated that PLD is a successful technique to impart bioactivity to implants for biomedical applications.

Table 3. Pulsed laser deposition (PLD) experimental details and investigated properties of films of BG and BGC.

BG and BGC Systems	Laser Source	Deposition Conditions	Substrate	Properties	Ref.
SiO ₂ -Na ₂ O-CaO-P ₂ O ₅ (45S5) ¹	532 nm, 7 ns, 10 Hz	0.5–14 J/cm ² , RT, 10 ⁻⁴ Pa	Ti4Al	Film adhesion	[106]
	532 nm, 7 ns, 10 Hz	0.5–14 J/cm ² , RT, 10 ⁻⁴ Pa	Ti6Al4V	Film adhesion and bioactivity in SBF	[107]
	532 nm, 7 ns, 10 Hz	9 J/cm ² , RT, 10 ⁻⁴ Pa	Ti6Al4V	Hardness	[112]
	248 nm, 20 ns, 10 Hz	4 J/cm ² , 20, 200 and 500 °C, 8.5 × 10 ⁻⁵ Pa, 55 mm, 1 h	Ti6Al4V	Film adhesion	[142]
	532 nm, 6 ns, 10 Hz	2 × 10 ⁻⁵ mbar, RT and 200 °C, 1 h	Ti-6Al-4V	Bioactivity in SBF and biocompatibility with U2OS osteosarcoma cells to	[154]
SiO ₂ -Na ₂ O-CaO-P ₂ O ₅ -(MgO) (45S5, Mg10) ²	248 nm, 20 ns, 10 Hz	4 J/cm ² , 200 °C, 8.5 × 10 ⁻⁵ Pa, 55 mm, 1 h	Ti6Al4V	Film adhesion and bioactivity in SBF	[166]
HA/45S5	248 nm, 20 ns, 5 Hz	5 J/cm ² , 200 and 600 °C, 3 × 10 ⁻⁵ Pa, 1 h	Ti-6Al-4V	Bioactivity in SBF and in vivo osteointegration	[153]
	248 nm, 20 ns, 5 Hz	5 J/cm ² , 600 °C, 3 × 10 ⁻⁵ Pa, 1 h	Ti-6Al-4V	Film adhesion strength, biocompatibility with L929 mouse fibroblast and in vivo osteointegration	[167]
SiO ₂ -Na ₂ O-K ₂ O-MgO-CaO-P ₂ O ₅ (BG42) ³	193 nm, 10 Hz	175 mJ, 200 °C	SiC	Bioactivity in SBF	[158]
	193 nm, 10 Hz	0.2–0.6 J/cm ² , 25–500 °C, 10 ⁻⁵ mbar, 35 mm	Si	Hardness and elastic modulus	[15]
	193 nm	4.17 J/cm ² , 200 °C	Si, Ti, SiC	Bioactivity in SBF	[159]
	193 nm, 25 ns, 10 Hz	4.17 J/cm ² , 200 °C	SiC	Bioactivity in SBF, biocompatibility with MG-63 osteoblast-like cells	[161]
SiO ₂ -Na ₂ O-K ₂ O-MgO-CaO-P ₂ O ₅ -(B ₂ O ₃) (BG42, BG50, BG55, BG59) ⁴	193 nm, 10 Hz	4.2 J/cm ² , 200 °C	Ti6Al4V, SiC	Bioactivity in SBF, biocompatibility, cell attachment and proliferation of MG-63 osteoblast-like cells	[160]
	193 nm, 10 Hz	4.2 J/cm ² , 200 °C	Ti	Bioactivity in SBF, biocompatibility in muscle tissue by an in vivo test	[149]
SiO ₂ -Na ₂ O-K ₂ O-MgO-CaO-P ₂ O ₅ (6P57) ⁵	248 nm, 7 ns, 2 Hz	400–550 °C, 5–15 Pa O ₂ , 4 cm	Ti	Biocompatibility and proliferation of Hek293 cells.	[104]
SiO ₂ -Na ₂ O-K ₂ O-MgO-CaO-P ₂ O ₅ (6P57, 6P61) ⁶	248 nm, 25 ns,	5.7 J/cm ² , 400 °C, 13 Pa O ₂ , 4 cm	Ti	Bioactivity in SBF and cell adhesion of human osteoblasts after SBF soaking	[138]
	248 nm, 25 ns,	5.7 J/cm ² , 400 °C, 13 Pa O ₂ , 4 cm	Ti	Biocompatibility and proliferation of osteoblast cells	[127]
	248 nm, ≥ 7 ns, 2 Hz	2.8 J/cm ² , 400 °C, 13 Pa O ₂	Etched Ti gr4d	Bioactivity in SBF	[129]
	248 nm, 25 ns, 5 Hz	6.6 J/cm ² , 400 °C, 13 Pa O ₂ , 4 cm	Ti	Bioactivity in SBF and corrosion resistance	[139]
SiO ₂ -Na ₂ O-K ₂ O-CaO-P ₂ O ₅ ⁷	1064 nm, 10 ns, 10 Hz,	10 J/cm ² , RT, 10 ⁻⁶ mbar, 4 cm,	Ti	Bioactivity in SBF	[114]
SiO ₂ -Na ₂ O-K ₂ O-CaO-MgO-P ₂ O ₅ -CaF ₂ -La ₂ O ₃ -Ta ₂ O ₅ (RKKP) ⁸	532 nm, 10 ns, 10 Hz	12–44 J/cm ² , RT–500 °C, 4 × 10 ⁻⁴ Pa, 2 cm, 2 h	Ti	Hardness	[111]
	532 nm, 10 ns, 10 Hz	12 J/cm ² , 500 °C, 4 × 10 ⁻⁴ Pa, 2 cm, 2 h	Ti	Adhesion, growth and osteogenic differentiation of CaCo-2 cells	[151]
	532 nm, 10 ns, 10 Hz	12 J/cm ² , 400 °C, 4 × 10 ⁻⁴ Pa, 2 cm, 2 h	Mg-Ca	Corrosion resistance	[164]
	532 nm, 10 ns, 10 Hz	12 J/cm ² , 500 °C, 1.5 × 10 ⁻⁴ Pa, 2 cm, 2 h	Ti	Biocompatibility, proliferation and osteogenic differentiation of hAMSCs grown	[152]

Table 3. Cont.

BG and BGC Systems	Laser Source	Deposition Conditions	Substrate	Properties	Ref.
RKKP + C ₆₀ (5 wt.%)	532 nm, 10 ns, 10 Hz	12 J/cm ² , RT, 300 and 500 °C, 4 × 10 ⁻⁴ Pa, 2 cm, 4 h	Ti	Hardness	[148]
RKKP-Mn ⁹	532 nm, 10 ns, 10 Hz	12 J/cm ² , RT and 500 °C, 4 × 10 ⁻⁴ Pa, 2 cm, 4 h	Ti	Bioactivity in SBF	[146]
CaO–MgO–P ₂ O ₅ –SiO ₂ ¹⁰	1064 nm, 7 ns, 10 Hz	200 mJ, 200 °C, 10 ⁻⁵ Pa, 40 mm, 60 min	Ti6Al4V	Film adhesion and bioactivity in SBF	[150]
	1064 nm, 7 ns, 10 Hz	200 mJ, 200 °C, 10 ⁻⁵ Pa, 40 mm, 60 min	Ti6Al4V treated with micro-arc oxidation	Film adhesion corrosion resistance and bioactivity in SBF	[157]
SiO ₂ –CaO–P ₂ O ₅ –CaF ₂ –MgO (HASi) ¹¹	355 nm, 10 Hz	1.6 J/cm ² , 400 °C, 10 ⁻³ mbar O ₂ , 35 mm, 1 h	Ti6Al4V	Film adhesion hardness and bioactivity in SBF	[126]
Ca ₂ MgSi ₂ O ₇ (AKT)	5 Hz	180 MJ, RT, 20 MPa O ₂ , 15, 25 and 40 min	PSU and PDLA films	Hardness and elastic modulus test, bioactivity in SBF, cell attachment and proliferation of MC3T3 cells, osteogenic and angiogenic ability	[133]
	5 Hz	180 MJ, RT, 20 MPa O ₂ , 40 min	PET sheets	Proliferation and osteogenic/angiogenic differentiation of the BMSCs, in vivo osseointegration	[120]
	5 Hz	180 MJ, RT, 20 MPa O ₂ , 30 min	PDLA/PCL electrospun scaffold	Proliferation of human umbilical vein endothelial cells (HUVECs) and in vivo wound healing	[134]
SiO ₂ –Na ₂ O–K ₂ O–MgO–CaO–P ₂ O ₅ (BG57) ¹²	248 nm, 25 ns, 10 Hz	400 °C, 13 Pa O ₂ , 4 cm	stainless steel 316L	Corrosion resistance, bioactivity in SBF, biocompatibility with WJ-MSCs (Wharton's Jelly-derived Mesenchymal Stromal Cells)	[140]
SiO ₂ –Na ₂ O–K ₂ O–MgO–CaO–P ₂ O ₅ (BG61) ¹³	248 nm, 25 ns, 10 Hz	3 J/cm ² , RT, 1.5 × 10 ⁻³ Pa O ₂	UHMWPE	Bioactivity in SBF	[137]
	248 nm, 25 ns, 10 Hz	2.8 J/cm ² , 400 °C, 13 Pa O ₂ , 4 cm	Ti, stainless steel 316L	Corrosion resistance, bioactivity in SBF, biocompatibility with WJ-MSCs	[141]
SiO ₂ –CaO–P ₂ O ₅ –(CaF ₂) ¹⁴	355 nm, 5 ns, 10 Hz	2.2–3.7 J/cm ² , 400 °C, 10 mTorr O ₂ , 4 cm	Ti	Biocompatibility with Human endothelial cells (EAhy926 cell line)	[132]
(Cu _{0.0x})(Ca _{0.25-0.0x})P _{0.05} Si _{0.75} (0Cu–BG, 2Cu–BG, 5Cu–BG) ¹⁵	5 Hz	160 MJ, RT, 20 MPa O ₂ , 40 min	Eggshell membrane	Hardness, attachment proliferation, and angiogenic expression of human umbilical vein endothelial cells (HUVECs), antibacterial activity and in vivo wound healing	[122]
(Cu _{0.0x})(Ca _{0.25-0.0x})P _{0.05} Si _{0.75} (0Cu–BG, 5Cu–BG) ¹⁵	5 Hz	160 mJ, RT, 20 mPa O ₂ , 40 min	PET sheet	Biocompatibility, adhesion and osteogenic/angiogenic differentiation of the rBMSCs, in vivo osteointegration	[121]
Ca _{0.25} P _{0.05} Si _{0.7} O _{5.2}	5 Hz	160 mJ, RT, 20 mPa O ₂ , 40 min	PDLA/PCL electrospun	Proliferation and attachment, angiogenic expression, in vivo wound healing	[123]
Ca ₂ ZnSi ₂ O ₇	5Hz	180 MJ, RT, 20 MPa O ₂	BioGide [®] collagen membrane	Osteogenic differentiation of BMSCs, in vitro and in vivo osteoimmunomodulatory properties	[135]
P ₂ O ₅ –Nb ₂ O ₅ –CaO–(CaF ₂) (NbP–BG)	355 nm, 6 ns, 10 Hz	50–100 mJ, 3 × 10 ⁻⁶ mbar, 5 min, 30 mm	Etched Ti	Adhesion and proliferation of MC3T3 cells	[108]

Table 3. Cont.

BG and BGC Systems	Laser Source	Deposition Conditions	Substrate	Properties	Ref.
SiO ₂ -Na ₂ O-K ₂ O-MgO-CaO-P ₂ O ₅ -CuO (Cu-BG) ¹⁶	532 nm, 10 ns, 10 Hz	12 J/cm ² , RT, 300 and 500 °C, 4 × 10 ⁻⁴ Pa, 2 cm, 4 h	Ti	Bioactivity in SBF and antibacterial activity	[144]
SiO ₂ -CaO-P ₂ O ₅ -ZnO-MgO and SiO ₂ -CaO-P ₂ O ₅ -ZnO-SrO ¹⁷	532 nm, 10 Hz	73–74 mJ/pulse, 25–300 °C, 100 mTorr O ₂ , 4 cm	Si	Bioactivity in SBF and cellular adhesion and proliferation of human fetal osteoblast cells	[119]
SiO ₂ -Na ₂ O-K ₂ O-MgO-CaO-P ₂ O ₅ -(B ₂ O ₃) (13-93, 19-93-B3) ¹⁸	532 nm, 7 ns, 10 Hz	12 J/cm ² , RT, 10 ⁻⁴ Pa, 2 cm, 5 h	Ti	Biocompatibility and osteogenic differentiation of Equine adipose tissue-derived mesenchymal stem cells (ADMSCs)	[155]
SiO ₂ -P ₂ O ₅ -CaO-MgO-Na ₂ O-CeO ₂ ¹⁹	355 nm	73–74 mJ/pulse, RT-300 °C, 100 mTorr O ₂ , 4 cm	Si	Bioactivity in SBF, biocompatibility with human fibroblast BJ cells and antibacterial activity	[128]
SiO ₂ -P ₂ O ₅ -CaO-MgO-Na ₂ O ²⁰	355 nm, 5 ns, 10 Hz	1.5 J/cm ² , RT-300 °C, 100 mTorr O ₂ , 4 cm	Si	Bioactivity in SBF and biocompatibility with human fibroblast BJ cells	[130]
SiO ₂ -P ₂ O ₅ -CaO-MgO-SrO-Na ₂ O ²¹	355 nm	73–74 mJ/pulse, RT-300 °C, 100 mTorr O ₂ , 4 cm	-	Bioactivity in SBF and biocompatibility with human fibroblast BJ cells	[136]
CaO-SiO ₂	-	84 mJ/pulse, 400 °C, 100 mTorr O ₂ ,	Ti	Film adhesion strength, biocompatibility with endothelial cells	[125]

¹ 45S5: 45 SiO₂-24.5 Na₂O-24.5 CaO-6 P₂O₅ (wt.%). ² Mg10: 45 SiO₂-14.5 Na₂O-24.5 CaO-6 P₂O₅-10 MgO (wt.%). ³ BG42: 42 SiO₂-20 Na₂O-10 K₂O-20 CaO-3 P₂O₅-5 MgO (wt.%). ⁴ BG50: 50 SiO₂-15 Na₂O-15 K₂O-15 CaO-2 MgO-3 B₂O₃ (wt.%). BG55: 55 SiO₂-21 Na₂O-9 K₂O-8 CaO-4 P₂O₅-2 MgO-1 B₂O₃ (wt.%). BG59: 59 SiO₂-10 Na₂O-5 K₂O-15 CaO-3 P₂O₅-5 MgO-3 B₂O₃ (wt.%). ⁵ 6P57: 56.5 SiO₂-11 Na₂O-3 K₂O-15 CaO-8.5 MgO-6 P₂O₅ (wt.%). ⁶ 6P61: 61.1 SiO₂-10.3 Na₂O-2.8 K₂O-12.6 CaO-7.2 MgO-6 P₂O₅ (wt.%). ⁷ 42.34 SiO₂-23.06 CaO-11.50 Na₂O-17.47 K₂O-5.63 P₂O₅ (wt.%). ⁸ RKKP: 43.68 SiO₂-11.10 P₂O₅-31.30 CaO-4.53 Na₂O-2.78 MgO-4.92 CaF₂-0.19 K₂O-0.50 La₂O₃-1.00 Ta₂O₅ (wt.%). ⁹ RKKP-Mn: 43.29 SiO₂-11.00 P₂O₅-31.02 CaO-4.49 Na₂O-2.76 MgO-4.88 CaF₂-0.19 K₂O-0.50 La₂O₃-0.99 Ta₂O₅-0.89 MnO (wt.%). ¹⁰ 28CaO-10MgO-4P₂O₅-58SiO₂ (mol%). ¹¹ 34.2 SiO₂-44.9 CaO-16.3 P₂O₅-0.5 CaF₂-4.6 MgO (wt.%). ¹² BG57 see 6P57. ¹³ BG61 see 6P61. ¹⁴ A: 60 SiO₂-36 CaO-4 P₂O₅ (mol%). B: 60 SiO₂-35.25 CaO-4 P₂O₅-0.75 CaF₂ (mol%). ¹⁵ 0Cu-BG: (0 mol% Cu), 2Cu-BG: (2 mol% Cu), 5Cu-BG: (5 mol% Cu). ¹⁶ Cu-BG: 45 SiO₂-24.5 Na₂O-19.5 CaO-6 P₂O₅-5 CuO (wt.%). ¹⁷ Composition-Mg: 60 SiO₂-25 CaO-5 P₂O₅-5 ZnO-5 MgO (mol%). Composition-Sr: 60 SiO₂-25 CaO-5 P₂O₅-5 ZnO-5 SrO (mol%). ¹⁸ 13-93: 5.5 Na₂O-11.1 K₂O-4.6 MgO-18.5 CaO-3.7 P₂O₅-56.6 SiO₂ (wt.%). 13-93-B3: 5.5 Na₂O-11.1 K₂O-4.6 MgO-18.5 CaO-3.7 P₂O₅-56.6 B₂O₃ (wt.%). ¹⁹ 46.10 SiO₂-2.60 P₂O₅-16.90 CaO-10.00 MgO-19.40 Na₂O-5.00 CeO₂ (mol.%). ²⁰ 46.1 SiO₂-2.6 P₂O₅-16.9 CaO-10.0 MgO-24.4 Na₂O (mol%). ²¹ 46.1SiO₂-2.6P₂O₅-16.9CaO-10MgO-5SrO-19.4Na₂O(mol%).

5. Conclusions

The results of several researches regarding the ns-PLD of substituted HA and bioactive glass and glass-ceramics have been reviewed. Thanks to in-depth studies on the deposition mechanism and film growth for these classes of materials, films with proper properties for biomedical applications have been produced. Several advantages were found by performing PLD of bioactive ceramics. It is an environment-friendly technique since no by-products are originated, and no solvent and toxic reagents are used. By controlling deposition parameters, it is possible to preserve the composition of the target material in the deposited film and control the film crystallization, thickness, morphology, and roughness.

Thanks to the possibility to deposit almost any material and different combinations on thermal degradable substrates of various shapes, any kind of implant surface can be modified in order to activate the desired biological response. A number of steps have been taken towards ceramics composition by adding ions that are able to impart enhanced osteogenic, angiogenic, and/or antibacterial properties by activating specific signal pathways once implanted in a living person.

Author Contributions: Conceptualization, R.T., M.C. and A.D.B.; original draft preparation, review and editing, R.T., M.C. and A.D.B. All authors have read and agreed to the published version of the manuscript.

Funding: This research received no external funding.

Institutional Review Board Statement: Not applicable.

Informed Consent Statement: Not applicable.

Data Availability Statement: Not applicable.

Conflicts of Interest: The authors declare no conflict of interest.

References

1. Fu, Y.; Cui, S.; Luo, D.; Liu, Y. Novel inorganic nanomaterial-based therapy for bone tissue regeneration. *Nanomaterials* **2021**, *11*, 789. [\[CrossRef\]](#)
2. Shi, H.; Zhou, Z.; Li, W.; Fan, Y.; Li, Z.; Wei, J. Hydroxyapatite based materials for bone tissue engineering: A brief and comprehensive introduction. *Crystals* **2021**, *11*, 149. [\[CrossRef\]](#)
3. Eliaz, N.; Metoki, N. Calcium phosphate bioceramics: A review of their history, structure, properties, coating technologies and biomedical applications. *Materials* **2017**, *10*, 334. [\[CrossRef\]](#)
4. Panneerselvam, R.; Anandhan, N.; Gopu, G.; Amali Roselin, A.; Ganesan, K.P.; Marimuthu, T. Impact of different transition metal ions in the structural, mechanical, optical, chemico-physical and biological properties of nanohydroxyapatite. *Appl. Surf. Sci.* **2020**, *506*, 144802. [\[CrossRef\]](#)
5. Sevenscan, A.; Doyuk, E.K.; Köse, N. Silver ion doped hydroxyapatite-coated titanium pins prevent bacterial colonization. *Jt. Dis. Relat. Surg.* **2021**, *32*, 35–41. [\[CrossRef\]](#) [\[PubMed\]](#)
6. Kamonwannasit, S.; Futralan, C.M.; Khemthong, P.; Butburee, T.; Karaphun, A.; Phatai, P. Synthesis of copper-silver doped hydroxyapatite via ultrasonic coupled sol-gel techniques: Structural and antibacterial studies. *J. Sol. Gel. Sci. Technol.* **2020**, *96*, 452–463. [\[CrossRef\]](#)
7. Wang, G.; Zreiqat, H. Functional coatings or films for hard-tissue applications. *Materials* **2010**, *3*, 3994–4050. [\[CrossRef\]](#)
8. Li, K.; Dai, F.; Yan, T.; Xue, Y.; Zhang, L.; Han, Y. Magnetic Silicium Hydroxyapatite nanorods for enhancing osteoblast response in vitro and biointegration in vivo. *ACS Biomater. Sci. Eng.* **2019**, *5*, 2208–2221. [\[CrossRef\]](#) [\[PubMed\]](#)
9. Hench, L.L. The story of Bioglass®. *J. Mater. Sci. Mater. Med.* **2006**, *17*, 967–978. [\[CrossRef\]](#)
10. Brauer, D.S. Bioactive Glasses-Structure and Properties. *Angew. Chem. Int. Ed.* **2015**, *54*, 4160–4181. [\[CrossRef\]](#)
11. Shelby, J.E. *Introduction to Glass Science and Technology*, 2nd ed.; Royal Society of Chemistry: Cambridge, UK, 2005. [\[CrossRef\]](#)
12. FitzGerald, V.; Pickup, D.M.; Greenspan, D.; Sarkar, G.; Fitzgerald, J.J.; Wetherall, K.M.; Moss, R.M.; Jones, J.R.; Newport, R.J. A neutron and X-ray diffraction study of bioglass® with reverse monte carlo modelling. *Adv. Funct. Mater.* **2007**, *17*, 3746–3753. [\[CrossRef\]](#)
13. Xiang, Y.; Du, J. Effect of strontium substitution on the structure of 45S5 bioglasses. *Chem. Mater.* **2011**, *23*, 2703–2717. [\[CrossRef\]](#)
14. Pedone, A.; Malavasi, G.; Menziani, C.M.; Segre, U.; Cormack, A.N. Role of magnesium in soda-lime glasses: Insight into structural, transport, and mechanical properties through computer simulations. *J. Phys. Chem. C* **2008**, *112*, 11034–11041. [\[CrossRef\]](#)
15. Serra, J.; Liste, S.; González, P.; Serra, C.; Borrajo, J.P.; Chiussi, S.; León, B.; Pérez-Amor, M. The role of the temperature and laser fluence on the properties of PLD bioactive glass films. *Appl. Phys. A Mater. Sci. Process* **2004**, *79*, 983–986. [\[CrossRef\]](#)
16. Ravaglioli, A.; Krajewski, A.; Baldi, G.; Tateo, F.; Peruzzo, L.; Piancastelli, A. Glass-ceramic scaffolds for tissue engineering. *Adv. Appl. Ceram.* **2008**, *107*, 268–273. [\[CrossRef\]](#)
17. El-Meliegy, E.; van Noort, R. *Glasses and Glass Ceramics for Medical Applications*; Springer: New York, NY, USA, 2012. [\[CrossRef\]](#)
18. Bose, S.; Tarafder, S.; Bandyopadhyay, A. Hydroxyapatite coatings for metallic implants. In *Hydroxyapatite (HAp) for Biomedical Applications*; Mucalo, M., Ed.; Elsevier Ltd.: Amsterdam, The Netherlands, 2015; Volume 7, pp. 143–157. [\[CrossRef\]](#)
19. Gittens, R.A.; Mclachlan, T.; Olivares-Navarrete, R.; Cai, Y.; Berner, S.; Tannenbaum, R.; Schwartz, Z.; Sandhage, K.H.; Boyan, B.D. The effects of combined micron-/submicron-scale surface roughness and nanoscale features on cell proliferation and differentiation. *Biomaterials* **2011**, *32*, 3395–3403. [\[CrossRef\]](#)
20. Im, B.J.; Lee, S.W.; Oh, N.; Lee, M.H.; Kang, J.H.; Leesungbok Ri Lee SCAhn, S.J.; Park, J.S. Texture direction of combined microgrooves and submicroscale topographies of titanium substrata influence adhesion, proliferation, and differentiation in human primary cells. *Arch. Oral Biol.* **2011**, *57*, 898–905. [\[CrossRef\]](#)
21. Cabañas, M.V. Bioceramic Coatings for Medical Implants. In *Bio-Ceramics with Clinical Applications*, 1st ed.; Vallet-Regí, M., Ed.; John Wiley & Sons Ltd.: Chichester, UK, 2014; Volume 9, pp. 249–289. [\[CrossRef\]](#)
22. Choi, G.; Choi, A.H.; Evans, L.A.; Akyol, S.; Ben-Nissan, B. A review: Recent advances in sol-gel-derived hydroxyapatite nanocoatings for clinical applications. *J. Am. Ceram. Soc.* **2020**, *103*, 5442–5453. [\[CrossRef\]](#)
23. Jaafar, A.; Hecker, C.; Árki, P.; Joseph, Y. Sol-gel derived hydroxyapatite coatings for titanium implants: A review. *Bioengineering* **2020**, *7*, 127. [\[CrossRef\]](#) [\[PubMed\]](#)
24. Awasthi, S.; Pandey, S.K.; Arunan, E.; Srivastava, C. A review on hydroxyapatite coatings for the biomedical applications: Experimental and theoretical perspectives. *J. Mater. Chem. B* **2021**, *9*, 228–249. [\[CrossRef\]](#)
25. Asri, R.I.M.; Harun, W.S.W.; Hassan, M.A.; Ghani, S.A.C.; Buyong, Z. A review of hydroxyapatite-based coating techniques: Sol-gel and electrochemical depositions on biocompatible metals. *J. Mech. Behav. Biomed. Mater.* **2016**, *57*, 95–108. [\[CrossRef\]](#)
26. Sun, L.; Berndt, C.C.; Gross, K.A.; Kucuk, A. Material fundamentals and clinical performance of plasma-sprayed hydroxyapatite coatings: A review. *J. Biomed. Mater. Res.* **2001**, *58*, 570–592. [\[CrossRef\]](#) [\[PubMed\]](#)

27. Ratha, I.; Datta, P.; Balla, V.K.; Nandi, S.K.; Kundu, B. Effect of doping in hydroxyapatite as coating material on biomedical implants by plasma spraying method: A review. *Ceram. Int.* **2021**, *47*, 4426–4445. [[CrossRef](#)]
28. Yang, Y.; Kim, K.H.; Ong, J.L. A review on calcium phosphate coatings produced using a sputtering process—An alternative to plasma spraying. *Biomaterials* **2005**, *26*, 327–337. [[CrossRef](#)] [[PubMed](#)]
29. Durham, J.W.; Allen, M.J.; Rabiei, A. Preparation, characterization and in vitro response of bioactive coatings on polyether ether ketone. *J. Biomed. Mater. Res. Part B Appl. Biomater.* **2017**, *105*, 560–567. [[CrossRef](#)] [[PubMed](#)]
30. Cui, F.Z.; Luo, Z.S. Biomaterials modification by ion-beam processing. *Surf. Coatings Technol.* **1999**, *112*, 278–285. [[CrossRef](#)]
31. Mohseni, E.; Zalnezhad, E.; Bushroa, A.R. Comparative investigation on the adhesion of hydroxyapatite coating on Ti-6Al-4V implant: A review paper. *Int. J. Adhes. Adhes.* **2014**, *48*, 238–257. [[CrossRef](#)]
32. Safavi, M.S.; Surmeneva, M.A.; Surmenev, R.A.; Khalil-Allafi, J. RF-magnetron sputter deposited hydroxyapatite-based composite & multilayer coatings: A systematic review from mechanical, corrosion, and biological points of view. *Ceram. Int.* **2021**, *47*, 3031–3053. [[CrossRef](#)]
33. Kozelskaya, A.I.; Kulkova, S.E.; Fedotkin, A.Y.; Bolbasov, E.N.; Zhukov, Y.M.; Stipnice, L.; Bakulin AVUseinov, A.S.; Shesterikov, E.V.; Locs, J.; et al. Radio frequency magnetron sputtering of Sr- and Mg-substituted β -tricalcium phosphate: Analysis of the physicochemical properties and deposition rate of coatings. *Appl. Surf. Sci.* **2020**, *509*, 144763. [[CrossRef](#)]
34. Surmenev, R.A. A review of plasma-assisted methods for calcium phosphate-based coatings fabrication. *Surf. Coat. Technol.* **2012**, *206*, 2035–2056. [[CrossRef](#)]
35. Nelea, V.; Morosanu, C.; Iliescu, M.; Mihailescu, I.N. Hydroxyapatite thin films grown by pulsed laser deposition and radio-frequency magnetron sputtering: Comparative study. *Appl. Surf. Sci.* **2004**, *228*, 346–356. [[CrossRef](#)]
36. Solla, E.L.; González, P.; Serra, J.; Chiussi, S.; León, B.; López, J.G. Pulsed laser deposition of silicon substituted hydroxyapatite coatings from synthetical and biological sources. *Appl. Surf. Sci.* **2007**, *254*, 1189–1193. [[CrossRef](#)]
37. Rau, J.V.; Cacciotti, I.; De Bonis, A.; Fosca, M.; Komlev, V.S.; Latini, A.; Santagata, A.; Teghil, R. Fe-doped hydroxyapatite coatings for orthopedic and dental implant applications. *Appl. Surf. Sci.* **2014**, *307*, 301–305. [[CrossRef](#)]
38. Rodríguez-Valencia, C.; Lopez-Álvarez, M.; Cochón-Cores, B.; Pereiro, I.; Serra, J.; González, P. Novel selenium-doped hydroxyapatite coatings for biomedical applications. *J. Biomed. Mater. Res. Part A* **2013**, *101A*, 853–861. [[CrossRef](#)] [[PubMed](#)]
39. Motoc, M.M.; Axente, E.; Popescu, C.; Sima, L.E.; Petrescu, S.M.; Mihailescu, I.N.; Gyorgy, E. Active protein and calcium hydroxyapatite bilayers grown by laser techniques for therapeutic applications. *J. Biomed. Mater. Res. Part A* **2013**, *101A*, 2706–2711. [[CrossRef](#)] [[PubMed](#)]
40. Popescu-Pelin, G.; Sima, F.; Sima, L.E.; Mihailescu, C.N.; Luculescu, C.; Iordache, I.; Socol, M.; Socol, G.; Mihailescu, I.N. Hydroxyapatite thin films grown by pulsed laser deposition and matrix assisted pulsed laser evaporation: Comparative study. *Appl. Surf. Sci.* **2017**, *418*, 580–588. [[CrossRef](#)]
41. Duta, L. In vivo assessment of synthetic and biological-derived calcium phosphate-based coatings fabricated by pulsed laser deposition: A review. *Coatings* **2021**, *11*, 99. [[CrossRef](#)]
42. De Bonis, A.; Teghil, R. Ultra-short pulsed laser deposition of oxides, borides and carbides of transition elements. *Coatings* **2020**, *10*, 501. [[CrossRef](#)]
43. Schneider, C.W.; Lippert, T. Laser Ablation and Thin Film Deposition. In *Laser Processing of Materials: Fundamentals, Applications and Developments*; Schaaf, P., Ed.; Springer: Berlin/Heidelberg, Germany, 2010; Volume 5, pp. 89–112.
44. Fähler, S.; Krebs, H.U. Calculations and experiments of material removal and kinetic energy during pulsed laser ablation of metals. *Appl. Surf. Sci.* **1996**, *96–98*, 61–65. [[CrossRef](#)]
45. Kelly, R.; Miotello, A.; Mele, A.; Giardini Guidoni, A. Plume Formation and Characterization in Laser-Surface Interactions. In *Experimental Methods in the Physical Sciences*; Miller, J.C., Haglund, R.F., Eds.; Academic Press by Elsevier: Cambridge, MA, USA, 1997; Volume 30, pp. 225–289. [[CrossRef](#)]
46. Miotello, A.; Kelly, R. Laser-induced phase explosion: New physical problems when a condensed phase approaches the thermodynamic critical temperature. *Appl. Phys. A Mater. Sci. Process.* **1999**, *69*, 67–73. [[CrossRef](#)]
47. Perez, D.; Lewis, L.J.; Lorazo, P.; Meunier, M. Ablation of molecular solids under nanosecond laser pulses: The role of inertial confinement. *Appl. Phys. Lett.* **2006**, *89*, 141907. [[CrossRef](#)]
48. Willmott, P.R.; Huber, J.R. Pulsed laser vaporization and deposition. *Rev. Mod. Phys.* **2000**, *2*, 315–328. [[CrossRef](#)]
49. Anisimov, S.I.; Luk'yanchuk, B.S.; Luches, A. An analytical model for three-dimensional laser plume expansion into vacuum in hydrodynamic regime. *Appl. Surf. Sci.* **1996**, *96–98*, 24–32. [[CrossRef](#)]
50. Lowndes, D.H. Growth and Doping of Compound Semiconductor Films by Pulsed Laser Ablation. In *Experimental Methods in the Physical Sciences*; Miller, J.C., Haglund, R.F., Eds.; Academic Press by Elsevier: Cambridge, MA, USA, 1997; Volume 30, pp. 475–571. [[CrossRef](#)]
51. Cotell, C.M.; Grabowski, K.S. Novel Materials Applications of Pulsed Laser Deposition. *MRS Bull* **1992**, *17*, 44–53. [[CrossRef](#)]
52. Cotell, C.M. Pulsed Laser Deposition and Processing of Biocompatible Hydroxylapatite Thin Films. *Appl. Surf. Sci.* **1993**, *69*, 140–148. [[CrossRef](#)]
53. Singh, R.K.; Qian, F.; Nagabushnam, V.; Damodaran, R.; Moudgil, B.M. Excimer laser deposition of hydroxyapatite thin films. *Biomaterials* **1994**, *15*, 522–528. [[CrossRef](#)]

54. Arias, J.L.; Garcíá-Sanz, F.J.; Mayor, M.B.; Chiussi, S.; Pou, J.; León, B.; Pérez-Amor, M. Physicochemical properties of calcium phosphate coatings produced by pulsed laser deposition at different water vapour pressures. *Biomaterials* **1998**, *19*, 883–888. [[CrossRef](#)]
55. Solla, E.L.; Borrajo, J.P.; González, P.; Serra, J.; Liste, S.; Chiussi, S.; León, B.; Pérez-Amor, M. Plasma assisted pulsed laser deposition of hydroxylapatite thin films. *Appl. Surf. Sci.* **2005**, *248*, 360–364. [[CrossRef](#)]
56. Nelea, V.; Ristoscu, C.; Chiritescu, C.; Ghica, C.; Mihailescu, I.N.; Pelletier, H.; Mille, P.; Cornet, A. Pulsed laser deposition of hydroxyapatite thin films on Ti-5Al-2.5Fe substrates with and without buffer layers. *Appl. Surf. Sci.* **2000**, *168*, 127–131. [[CrossRef](#)]
57. Arias, J.L.; Mayor, M.B.; Pou, J.; León, B.; Pérez-Amor, M. Stoichiometric transfer in pulsed laser deposition of hydroxylapatite. *Appl. Surf. Sci.* **2000**, *154–155*, 434–438. [[CrossRef](#)]
58. Baeri, P.; Torrisi, L.; Marino, N.; Foti, G. Ablation of hydroxyapatite by pulsed laser irradiation. *Appl. Surf. Sci.* **1992**, *54*, 210–214. [[CrossRef](#)]
59. Serra, P.; Palau, J.; Varela, A.; Esteve, J.; Morenza, J.L. Characterization of hydroxyapatite laser ablation plumes by fast intensified CCD-imaging. *J. Mater. Res.* **1995**, *10*, 473–478. [[CrossRef](#)]
60. Zeng, H.; Lacefield, W.R.; Mirov, S. Structural and morphological study of pulsed laser deposited calcium phosphate bioceramic coatings: Influence of deposition conditions, laser parameters, and target properties. *J. Biomed. Mater. Res.* **2000**, *50*, 248–258. [[CrossRef](#)]
61. Serra, P.; Clèries, L.; Morenza, J.L. Analysis of the expansion of hydroxyapatite laser ablation plumes. *Appl. Surf. Sci.* **1996**, *96–98*, 216–221. [[CrossRef](#)]
62. Serra, P.; Fernandez-Pradas, J.M.; Sardin, G.; Morenza, J.L. Interaction Effects of an Excimer Laser Beam with Hydroxyapatite Targets. *Appl. Surf. Sci.* **1997**, *109*, 384–388. [[CrossRef](#)]
63. Serra, P.; Morenza, J.L. Fluence dependence of hydroxyapatite laser ablation plumes. *Thin Solid Films* **1998**, *335*, 43–48. [[CrossRef](#)]
64. Agop, M.; Cimpoesu, N.; Gurlui, S.; Irimiciu, S.A. Investigations of transient plasma generated by laser ablation of hydroxyapatite during the pulsed laser deposition process. *Symmetry* **2020**, *12*, 132. [[CrossRef](#)]
65. Nishikawa, H.; Hasegawa, T.; Miyake, A.; Tashiro, Y.; Hashimoto, Y.; Blank, D.H.A.; Rijnders, G. Relationship between the Ca/P ratio of hydroxyapatite thin films and the spatial energy distribution of the ablation laser in pulsed laser deposition. *Mater. Lett.* **2016**, *165*, 95–98. [[CrossRef](#)]
66. Tri, L.Q.; Chua, D.H.C. An investigation into the effects of high laser fluence on hydroxyapatite/calcium phosphate films deposited by pulsed laser deposition. *Appl. Surf. Sci.* **2009**, *256*, 76–80. [[CrossRef](#)]
67. Gomes, G.C.; Borghi, F.F.; Ospina, R.O.; López, E.O.; Borges, F.O.; Mello, A. Nd:YAG (532 nm) pulsed laser deposition produces crystalline hydroxyapatite thin coatings at room temperature. *Surf. Coat. Technol.* **2017**, *329*, 174–183. [[CrossRef](#)]
68. Checca, N.R.; Borghi, F.F.; Rossi, A.M.; Mello, A.; Rossi, A.L. Nanostructure of calcium phosphate films synthesized by pulsed laser deposition under 1 Torr: Effect of wavelength and laser energy. *Appl. Surf. Sci.* **2021**, *545*, 148880. [[CrossRef](#)]
69. Bao, Q.; Chen, C.; Wang, D.; Liu, J. The influences of target properties and deposition times on pulsed laser deposited hydroxyapatite films. *Appl. Surf. Sci.* **2008**, *255*, 619–621. [[CrossRef](#)]
70. Guillot-Noël, O.; Gomez-San Roman, R.; Perrière, J.; Hermann, J.; Craciun, V.; Boulmer-Leborgne, C.; Barboux, P. Growth of apatite films by laser ablation: Reduction of the droplet areal density. *J. Appl. Phys.* **1996**, *80*, 1803–1808. [[CrossRef](#)]
71. György, E.; Toricelli, P.; Socol, G.; Iliescu, M.; Mayer, I.; Mihailescu, I.N.; Bigi, A.; Werckman, J. Biocompatible Mn²⁺-doped carbonated hydroxyapatite thin films grown by pulsed laser deposition. *J. Biomed. Mater. Res. Part A* **2004**, *71*, 353–358. [[CrossRef](#)] [[PubMed](#)]
72. Rau, J.V.; Generosi, A.; Laureti, S.; Komlev Vladimir, S.; Ferro, D.; Cesaro, S.N.; Paci, B.; Rossi Albertini, V.; Agostinelli, E.; Barinov, S.M. Physicochemical investigation of pulsed laser deposited carbonated hydroxyapatite films on titanium. *ACS Appl. Mater. Interfaces.* **2009**, *1*, 1813–1820. [[CrossRef](#)]
73. Okazaiki, M. Crystallographic behaviour of fluoridated hydroxyapatites containing Mg²⁺ and CO₃²⁻ ions. *Biomaterials* **1991**, *12*, 831–835. [[CrossRef](#)]
74. Mróz, W.; Jedyński, M.; Prokopiuk, A.; Ślósarczyk, A.; Paszkiewicz, Z. Characterization of calcium phosphate coatings doped with Mg, deposited by pulsed laser deposition technique using ArF excimer laser. *Micron* **2009**, *40*, 140–142. [[CrossRef](#)] [[PubMed](#)]
75. Mróz, W.; Bombalska, A.; Burdyńska, S.; Jedyński, M.; Prokopiuk, A.; Budner, B.; Ślósarczyk, A.; Zima, A.; Menaszek, E.; Ścisłowska-Czarnecka, A.; et al. Structural studies of magnesium doped hydroxyapatite coatings after osteoblast culture. *J. Mol. Struct.* **2010**, *977*, 145–152. [[CrossRef](#)]
76. Mróz, W.; Budner, B.; Syroka, R.; Niedzielski, K.; Golański, G.; Ślósarczyk, A.; Schwarze, D.; Douglas, T.E.L. In vivo implantation of porous titanium alloy implants coated with magnesium-doped octacalcium phosphate and hydroxyapatite thin films using pulsed laser deposition. *J. Biomed. Mater. Res. Part B Appl. Biomater.* **2015**, *103*, 151–158. [[CrossRef](#)] [[PubMed](#)]
77. Vandrovцова, M.; Douglas, T.E.L.; Mróz, W.; Musial, O.; Schaubroeck, D.; Budner, B.; Syroka, R.; Dubruel, P.; Bacakova, L. Pulsed laser deposition of magnesium-doped calcium phosphate coatings on porous polycaprolactone scaffolds produced by rapid prototyping. *Mater. Lett.* **2015**, *148*, 178–183. [[CrossRef](#)]
78. Graziani, G.; Bianchi, M.; Sassoni, E.; Russo, A.; Marcacci, M. Ion-substituted calcium phosphate coatings deposited by plasma-assisted techniques: A review. *Mater. Sci. Eng. C* **2017**, *74*, 219–229. [[CrossRef](#)]
79. Ferro, D.; Barinov, S.M.; Rau, J.V.; Teghil, R.; Latini, A. Calcium phosphate and fluorinated calcium phosphate coatings on titanium deposited by Nd:YAG laser at a high fluence. *Biomaterials* **2005**, *26*, 805–812. [[CrossRef](#)] [[PubMed](#)]

80. Rau, J.V.; Smirnov, V.V.; Laureti, S.; Generosi, A.; Varvaro, G.; Fosca, M.; Ferro, D.; Cesaro, N.; Rossi Albertini, V.; Barinov, S.M. Properties of pulsed laser deposited fluorinated hydroxyapatite films on titanium. *Mater. Res. Bull.* **2010**, *45*, 1304–1310. [[CrossRef](#)]
81. Cao, J.; Lian, R.; Jiang, X.; Liu, X. Formation of Porous Apatite Layer after Immersion in SBF of Fluorine-Hydroxyapatite Coatings by Pulsed Laser Deposition Improved in Vitro Cell Proliferation. *ACS Appl. Bio. Mater.* **2020**, *3*, 3698–3706. [[CrossRef](#)]
82. Hashimoto, Y.; Ueda, M.; Kohiga, Y.; Imura, K.; Hontsu, S. Application of fluoridated hydroxyapatite thin film coatings using KrF pulsed laser deposition. *Dent. Mater. J.* **2018**, *37*, 408–413. [[CrossRef](#)] [[PubMed](#)]
83. Cao, J.; Lian, R.; Jiang, X. Magnesium and fluoride doped hydroxyapatite coatings grown by pulsed laser deposition for promoting titanium implant cytocompatibility. *Appl. Surf. Sci.* **2020**, *515*, 146069. [[CrossRef](#)]
84. Montesi, M.; Panserì, S.; Dapporto, M.; Tampieri, A.; Sprio, S. Sr-substituted bone cements direct mesenchymal stem cells, osteoblasts and osteoclasts fate. *PLoS ONE* **2017**, *12*, e0172100. [[CrossRef](#)]
85. Capuccini, C.; Torricelli, P.; Sima, F.; Boanini, E.; Ristoscu, C.; Bracci, B.; Socol, G.; Fini, M.; Mihailescu, I.N.; Bigi, A. Strontium-substituted hydroxyapatite coatings synthesized by pulsed-laser deposition: In vitro osteoblast and osteoclast response. *Acta Biomater.* **2008**, *4*, 1885–1893. [[CrossRef](#)]
86. Pereiro, I.; Rodríguez-Valencia, C.; Serra, C.; Solla, E.L.; Serra, J.; González, P. Pulsed laser deposition of strontium-substituted hydroxyapatite coatings. *Appl. Surf. Sci.* **2012**, *258*, 9192–9197. [[CrossRef](#)]
87. De Bonis, A.; Uskoković, V.; Barbaro, K.; Fadeeva, I.; Curcio, M.; Imperatori, L.; Teghil, R.; Rau, J.V. Pulsed laser deposition temperature effects on strontium-substituted hydroxyapatite thin films for biomedical implants. *Cell Biol. Toxicol.* **2020**, *36*, 537–551. [[CrossRef](#)]
88. Solla, E.L.; Borrajo, J.P.; González, P.; Serra, J.; Chiussi, S.; León, B.; García López, J. Study of the composition transfer in the pulsed laser deposition of silicon substituted hydroxyapatite thin films. *Appl. Surf. Sci.* **2007**, *253*, 8282–8286. [[CrossRef](#)]
89. Solla, E.L.; Borrajo, J.P.; González, P.; Serra, J.; Chiussi, S.; Cerra, S.; Leon, B.; Perez-Amor, M. Pulsed laser deposition of silicon-substituted hydroxyapatite coatings. *Vacuum* **2008**, *82*, 1383–1385. [[CrossRef](#)]
90. López-Álvarez, M.; Solla, E.L.; González, P.; Serra, J.; Chiussi, S.; Serra, C.; León, B.; Pérez-Amor, M. Silicon-hydroxyapatite bioactive coatings (Si-HA) from diatomaceous earth and silica. Study of adhesion and proliferation of osteoblast-like cells. *J. Mater. Sci. Mater. Med.* **2009**, *20*, 1131–1136. [[CrossRef](#)] [[PubMed](#)]
91. Rau, J.V.; Fosca, M.; Cacciotti, I.; Laureti, S.; Bianco, A.; Teghil, R. Nanostructured Si-substituted hydroxyapatite coatings for biomedical applications. *Thin Solid Films* **2013**, *543*, 167–170. [[CrossRef](#)]
92. Rau, J.V.; Cacciotti, I.; Laureti, S.; Fosca, M.; Varvaro, G.; Latini, A. Bioactive, nanostructured Si-substituted hydroxyapatite coatings on titanium prepared by pulsed laser deposition. *J. Biomed. Mater. Res. Part B Appl. Biomater.* **2015**, *103*, 1621–1631. [[CrossRef](#)] [[PubMed](#)]
93. Rodríguez-Valencia, C.; Pereiro, I.; Pirraco, R.P.; López-Álvarez, M.; Serra, J.; González PMarques, A.P.; Reis, R.L. Human mesenchymal stem cells response to multi-doped silicon-strontium calcium phosphate coatings. *J. Biomater. Appl.* **2014**, *28*, 1397–1407. [[CrossRef](#)] [[PubMed](#)]
94. Wei, P.; Fang, J.; Fang, L.; Wang, K.; Lu, X.; Ren, F. Novel niobium and silver toughened hydroxyapatite nanocomposites with enhanced mechanical and biological properties for load-bearing bone implants. *Appl. Mater. Today* **2019**, *15*, 531–542. [[CrossRef](#)]
95. Jelínek, M.; Kocourek, T.; Jurek, K.; Remsa, J.; Mikšovský, J.; Weiserová, M.; Strnad, J.; Luxbacher, T. Antibacterial properties of Ag-doped hydroxyapatite layers prepared by PLD method. *Appl. Phys. A Mater. Sci. Process.* **2010**, *101*, 615–620. [[CrossRef](#)]
96. Sygnatowicz, M.; Keyshar, K.; Tiwari, A. Antimicrobial properties of silver-doped hydroxyapatite nano-powders and tin films. *Biol. Biomed. Mater.* **2010**, *62*, 65–70.
97. Kotoka, R.; Yamoah, N.K.; Mensah-Darkwa, K.; Moses, T.; Kumar, D. Electrochemical corrosion behavior of silver doped tricalcium phosphate coatings on magnesium for biomedical application. *Surf. Coat. Technol.* **2016**, *292*, 99–109. [[CrossRef](#)]
98. Mihailescu, I.N.; Torricelli, P.; Bigi, A.; Mayer, I.; Iliescu, M.; Wreckmann, J.; Socol, G.; Miroiu, F.; Cuisinier, F.; Elkaim, R.; et al. Calcium phosphate thin films synthesized by pulsed laser deposition: Physico-chemical characterization and in vitro cell response. In *Applied Surface Science*; Elsevier: Amsterdam, The Netherlands, 2005; Volume 248, pp. 344–348. [[CrossRef](#)]
99. Bigi, A.; Bracci, B.; Cuisinier, F.; Elkaim, R.; Fini, M.; Mayer, I.; Mihailescu, I.N.; Socol, G.; Sturba, L.; Torricelli, P. Human osteoblast response to pulsed laser deposited calcium phosphate coatings. *Biomaterials* **2005**, *26*, 2381–2389. [[CrossRef](#)] [[PubMed](#)]
100. Curcio, M.; Rau, J.V.; Santagata, A.; Teghil, R.; Laureti, S.; De Bonis, A. Laser synthesis of iron nanoparticle for Fe doped hydroxyapatite coatings. *Mater. Chem. Phys.* **2019**, *225*, 365–370. [[CrossRef](#)]
101. Antoniac, I.V.; Filipescu, M.; Barbaro, K.; Bonciu, A.; Birjega, R.; Cotrut, C.M.; Galvano, E.; Fosca, M.; Fadeeva, I.V.; Vadalà, G.; et al. Iron ion-doped tricalcium phosphate coatings improve the properties of biodegradable magnesium alloys for biomedical implant application. *Adv. Mater. Interfaces* **2020**, *7*, 2000531. [[CrossRef](#)]
102. Hidalgo-Robatto, B.M.; López-Álvarez, M.; Azevedo, A.S.; Dorado, J.; Serra, J.; Azevedo, N.F.; González, P. Pulsed laser deposition of copper and zinc doped hydroxyapatite coatings for biomedical applications. *Surf. Coat. Technol.* **2018**, *333*, 168–177. [[CrossRef](#)]
103. Ahmed, M.K.; Ramadan, R.; Afifi, M.; Menazea, A.A. Au-doped carbonated hydroxyapatite sputtered on alumina scaffolds via pulsed laser deposition for biomedical applications. *J. Mater. Res. Technol.* **2020**, *9*, 8854–8866. [[CrossRef](#)]
104. Gyorgy, E.; Grigorescu, S.; Socol, G.; Mihailescu, I.N.; Janackovic, D.; Dindune, A.; Kanepe, Z.; Palcevskis, E.; Zdrentu, E.L.; Petrescu, S.M. Bioactive glass and hydroxyapatite thin films obtained by pulsed laser deposition. *Appl. Surf. Sci.* **2007**, *253*, 7981–7986. [[CrossRef](#)]

105. Eraković, S.; Janković, A.; Ristoscu, C.; Duta, L.; Serban, N.; Visan, A.; Mihailescu, I.N.; Stan, G.E.; Socol, M.; Iordache, O.; et al. Antifungal activity of Ag:hydroxyapatite thin films synthesized by pulsed laser deposition on Ti and Ti modified by TiO₂ nanotubes substrates. *Appl. Surf. Sci.* **2014**, *293*, 37–45. [[CrossRef](#)]
106. D'Alessio, L.; Teghil, R.; Zaccagnino, M.; Zaccardo, I.; Ferro, D.; Marotta, V. Pulsed laser ablation and deposition of bioactive glass as coating material for biomedical applications. *Appl. Surf. Sci.* **1999**, *138–139*, 527–532. [[CrossRef](#)]
107. D'Alessio, L.; Ferro, D.; Marotta, V.; Santagata, A.; Teghil, R.; Zaccagnino, M. Laser ablation and deposition of Bioglass® 45S5 thin films. *Appl. Surf. Sci.* **2001**, *183*, 10–17. [[CrossRef](#)]
108. Sanz, C.K.; dos Santos, A.R.; da Silva, M.H.P.; Marçal, R.; Tute, E.M.; Meza, E.L.; Mello, A.; Borghi, F.F.; de Souza Camargo, S.A. Niobo-phosphate bioactive glass films produced by pulsed laser deposition on titanium surfaces for improved cell adhesion. *Ceram. Int.* **2019**, *45*, 18052–18058. [[CrossRef](#)]
109. Floroian, L.; Savu, B.; Sima, F.; Mihailescu, I.N.; Tanaskovic, D.; Janackovic, D. Synthesis and characterization of bioglass thin films. *Dig. J. Nanomater. Biostructures* **2007**, *2*, 285–291.
110. Liste, S.; González, P.; Serra, J.; Borrajo, J.P.; Chiussi, S.; Leon, B.; Perez-Amor, M.; Garcia-Lopez, J.; Ferrer, F.J.; Morilla, Y.; et al. Study of the stoichiometry transfer in pulsed laser deposition of bioactive silica-based glasses. *Thin Solid Films* **2004**, *453–454*, 219–223. [[CrossRef](#)]
111. Rau, J.V.; Teghil, R.; Fosca, M.; De Bonis, A.; Cacciotti, I.; Bianco, A.; Rossi Albertini, V.; Caminiti, R.; Ravaglioli, A. Bioactive glass-ceramic coatings prepared by pulsed laser deposition from RKKP targets (sol-gel vs melt-processing route). *Mater. Res. Bull.* **2012**, *47*, 1130–1137. [[CrossRef](#)]
112. Teghil, R.; Ferro, D.; Barinov, S.M. Hardness of bioactive glass film deposited on titanium alloy by pulsed laser ablation Certain glasses which contain specific amounts of SiO₂. *J. Mater. Sci. Lett.* **2002**, *21*, 379–382. [[CrossRef](#)]
113. Borrajo, J.P.; González, P.; Liste, S.; Serra, J.; Chiussi, S.; León, B.; Pérez-Amor, M. Pulsed laser deposition of bioactive glass films in ammonia and disilane atmospheres. *Appl. Surf. Sci.* **2005**, *248*, 369–375. [[CrossRef](#)]
114. Kwiatkowska, J.; Suchanek, K.; Rajchel, B. Bioactive glass coatings synthesized by pulsed laser deposition. *Tech. Acta Phys. Pol. A* **2012**, *121*, 502–505. [[CrossRef](#)]
115. González, P.; Serra, J.; Liste, S.; Chiussi, S.; León, B.; Pérez-Amor, M. Ageing of pulsed-laser-deposited bioactive glass films. *Vacuum* **2002**, *67*, 647–651. [[CrossRef](#)]
116. Liste, S.; Serra, J.; González, P.; Borrajo, J.P.; Chiussi, S.; León, B.; Pérez-Amor, M. The role of the reactive atmosphere in pulsed laser deposition of bioactive glass films. *Thin Solid Films* **2004**, *453–454*, 224–228. [[CrossRef](#)]
117. Solla, E.L.; Borrajo, J.P.; González, P.; Serra, J.; Liste, S.; Chiussi, S.; León, B.; Pérez-Amor, M. Nuevas tecnologías en el procesamiento de recubrimientos de cerámicas bioactivas. *Bol. Soc. Esp. Ceram. V* **2006**, *45*, 65–69. [[CrossRef](#)]
118. Zhao, Y.; Song, M.; Chen, C.; Liu, J. The role of the pressure in pulsed laser deposition of bioactive glass films. *J. Non Cryst. Solids* **2008**, *354*, 4000–4004. [[CrossRef](#)]
119. Jinga, S.I.; Toma, V.P.; Constantinoiu, I.; Banciu, A.; Banciu, D.D.; Busuioc, C. Development of new Mg-or Sr-containing bioactive interfaces to stimulate osseointegration of metallic implants. *Appl. Sci.* **2020**, *10*, 6647. [[CrossRef](#)]
120. Li, H.; Wu, C.; Chang, J.; Ge, Y.; Chen, S. Functional Polyethylene Terephthalate with Nanometer-Sized Bioactive Glass Coatings Stimulating in Vitro and in Vivo Osseointegration for Anterior Cruciate Ligament Reconstruction. *Adv. Mater. Interfaces* **2014**, *1*, 1400027. [[CrossRef](#)]
121. Li, H.; Li, J.; Jiang, J.; Lv, F.; Chang, J.; Chen, S.; Wu, C. An osteogenesis/angiogenesis-stimulation artificial ligament for anterior cruciate ligament reconstruction. *Acta Biomater.* **2017**, *54*, 399–410. [[CrossRef](#)] [[PubMed](#)]
122. Li, J.; Zhai, D.; Lv, F.; Yu, Q.; Ma, H.; Yin, J.; Yi, Z.; Liu, M.; Chang, J.; Wu, C. Preparation of copper-containing bioactive glass/eggshell membrane nanocomposites for improving angiogenesis, antibacterial activity and wound healing. *Acta Biomater.* **2016**, *36*, 254–266. [[CrossRef](#)]
123. Li, J.; Lv, F.; Xu, H.; Zhang, Y.; Wang, J.; Yi, Z.; Yin, J.; Chang, J.; Wu, C. A patterned nanocomposite membrane for high-efficiency healing of diabetic wound. *J. Mater. Chem. B* **2017**, *5*, 1926–1934. [[CrossRef](#)]
124. Mihailescu, N.; Stan, G.E.; Ristoscu, C.; Sopronyi, M.; Mihailescu, I.N. Bioactive glass thin films synthesized by advanced pulsed laser techniques. *J. Phys. Conf. Ser.* **2016**, *764*, 012020. [[CrossRef](#)]
125. Miu, D.M.; Jinga, S.I.; Voicu, G.; Iordache, F. Characteristics of wollastonite ceramic coatings obtained by pulsed laser deposition. *J. Inorg. Organomet. Polym. Mater.* **2020**, *4*, 1601–1607. [[CrossRef](#)]
126. Palangadan, R.; Sukumaran, A.; Fernandez, F.B.; John, A.; Varma, H. Pulsed laser deposition and in vitro characteristics of triphasic—HASi composition on titanium. *J. Biomater. Appl.* **2014**, *28*, 849–858. [[CrossRef](#)] [[PubMed](#)]
127. Popescu, A.C.; Sima, F.; Duta, L.; Popescu, C.; Mihailescu, I.N.; Capitanu, D.; Mustata, R.; Sima, L.E.; Petrescu, S.M.; Janackovic, D. Biocompatible and bioactive nanostructured glass coatings synthesized by pulsed laser deposition: In vitro biological tests. *Appl. Surf. Sci.* **2009**, *255*, 5486–5490. [[CrossRef](#)]
128. Prefac, G.A.; Milea, M.L.; Vadureanu, A.M.; Muraru, S.; Dobrin, D.I.; Isopencu, G.O.; Jinga, S.I.; Raileanu, M.; Bacalum, M.; Busuioc, C. CeO₂ containing thin films as bioactive coatings for orthopaedic implants. *Coatings* **2020**, *10*, 642. [[CrossRef](#)]
129. Berbecaru, C.; Alexandru, H.V.; Ianculescu, A.; Popescu, A.; Socol, G.; Sima, F. Mihailescu, Ion Bioglass thin films for biomimetic implants. *Appl. Surf. Sci.* **2009**, *255*, 5476–5479. [[CrossRef](#)]

130. Schitea, R.I.; Nitu, A.; Ciobota, A.A.; Munteanu, A.L.; David, I.M.; Miu, D.; Raileanu, M.; Bacalum, M.; Busuioc, C. Pulsed laser deposition derived bioactive glass-ceramic coatings for enhancing the biocompatibility of scaffolding materials. *Materials* **2020**, *13*, 2615. [[CrossRef](#)]
131. Tanaskovic, D.; Jokic, B.; Socol, G.; Popescu, A.; Mihailescu, I.N.; Petrovic, R.; Janackovic, D. Synthesis of functionally graded bioactive glass-apatite multistructures on Ti substrates by pulsed laser deposition. *Appl. Surf. Sci.* **2007**, *254*, 1279–1282. [[CrossRef](#)]
132. Voicu, G.; Miu, D.; Dogaru, I.; Jinga, S.I.; Busuioc, C. Vitroceramic interface deposited on titanium substrate by pulsed laser deposition method. *Int. J. Pharm* **2016**, *510*, 449–456. [[CrossRef](#)] [[PubMed](#)]
133. Wu, C.; Zhai, D.; Ma, H.; Li, X.; Zhang, Y.; Zhou, Y.; Luo, Y.; Wang, Y.; Xiao, Y.; Chang, J. Stimulation of osteogenic and angiogenic ability of cells on polymers by pulsed laser deposition of uniform akermanite-glass nanolayer. *Acta Biomater.* **2014**, *10*, 3295–3306. [[CrossRef](#)]
134. Xu, H.; Lv, F.; Zhang, Y.; Yi, Z.; Ke, Q.; Wu, C.; Liu, M.; Chang, J. Hierarchically micro-patterned nanofibrous scaffolds with a nanosized bio-glass surface for accelerating wound healing. *Nanoscale* **2015**, *7*, 18446–18452. [[CrossRef](#)] [[PubMed](#)]
135. Chen, Z.; Chen, L.; Liu, R.; Lin, Y.; Chen, S.; Lu, S.; Lin, Z.; Chen, Z.; Wu, C.; Xiao, Y. The osteoimmunomodulatory property of a barrier collagen membrane and its manipulation: Via coating nanometer-sized bioactive glass to improve guided bone regeneration. *Biomater. Sci.* **2018**, *6*, 1007–1019. [[CrossRef](#)] [[PubMed](#)]
136. Draghici, D.A.; Mihai, A.A.; Aioanei, M.O.; Negru, N.E.; Nicoara, A.I.; Jinga, S.I.; Miu, D.; Bacalum, M.; Busuioc, C. Strontium-Substituted Bioactive Glass-Ceramic Films for Tissue Engineering. *Bol. Soc. Esp. Ceram. V* **2020**, in press. [[CrossRef](#)]
137. Duta, L.; Popa, A.C.; Miculescu, F.; Mihailescu, I.N. Ultra high molecular weight polyethylene acetabular cups functionalized with bioactive glass coatings synthesized by pulsed laser deposition. *Rom. Reports Phys.* **2014**, *66*, 788–800.
138. Floroian, L.; Savu, B.; Stanciu, G.; Popescu, A.C.; Sima, F.; Mihailescu, I.N.; Mustata, R.; Sima, L.E.; Petrescu, S.M.; Tanaskovic, D.; et al. Nanostructured bioglass thin films synthesized by pulsed laser deposition: CSLM, FTIR investigations and in vitro biotests. *Appl. Surf. Sci.* **2008**, *255*, 3056–3062. [[CrossRef](#)]
139. Floroian, L.; Florescu, M.; Sima, F.; Popescu-Pelin, G.; Ristoscu, C.; Mihailescu, I.N. Synthesis of biomaterial thin films by pulsed laser technologies: Electrochemical evaluation of bioactive glass-based nanocomposite coatings for biomedical applications. *Mater. Sci. Eng. C* **2012**, *32*, 1152–1157. [[CrossRef](#)]
140. Floroian, L.; Florescu, M.; Munteanu, D.; Badea, M.; Popescu-Pelin, G.; Ristoscu, C.; Sima, F.; Chifiriuc, M.C.; Mihailescu, I.N. A new concept of stainless steel medical implant based upon composite nanostructures coating. *Dig. J. Nanomater. Biostructures* **2014**, *9*, 1555–1568.
141. Floroian, L.; Samoila, C.; Badea, M.; Munteanu, D.; Ristoscu, C.; Sima, F.; Negut, I.; Chifiriuc, M.C.; Mihailescu, I.N. Stainless steel surface biofunctionalization with PMMA-bioglass coatings: Compositional, electrochemical corrosion studies and microbiological assay. *J. Mater. Sci. Mater. Med.* **2015**, *26*, 195. [[CrossRef](#)]
142. Zhao, Y.; Song, M.; Chen, C.; Liu, J. Effects of the substrate temperature on the bioglass films deposited by pulsed laser. *Appl. Surf. Sci.* **2008**, *254*, 6897–6901. [[CrossRef](#)]
143. De Bonis, A.; Curcio, M.; Fosca, M.; Cacciotti, I.; Santagata, A.; Teghil, R.; Rau, J.V. RBP1 bioactive glass-ceramic films obtained by Pulsed Laser Deposition. *Mater. Lett.* **2016**, *175*, 195–198. [[CrossRef](#)]
144. Rau, J.V.; Curcio, M.; Raucchi, M.G.; Barbaro, K.; Fasolino, I.; Teghil, R.; Ambrosio, L.; De Bonis, A.; Boccaccini, A.R. Cu-Releasing Bioactive Glass Coatings and Their in Vitro Properties. *ACS Appl. Mater. Interfaces* **2019**, *11*, 5812–5820. [[CrossRef](#)]
145. Baino, F.; Novajra, G.; Miguez-Pacheco, V.; Boccaccini, A.R.; Vitale-Brovarone, C. Bioactive glasses: Special applications outside the skeletal system. *J. Non Cryst. Solids* **2016**, *432*, 15–30. [[CrossRef](#)]
146. Curcio, M.; De Stefanis, A.; De Bonis, A.; Teghil, R.; Rau, J.V. Pulsed laser deposited bioactive RKKP-Mn glass-ceramic coatings on titanium. *Surf. Coatings Technol.* **2019**, *357*, 122–128. [[CrossRef](#)]
147. Kokubo, T.; Takadama, H. How useful is SBF in predicting in vivo bone bioactivity? *Biomaterials* **2006**, *27*, 2907–2915. [[CrossRef](#)]
148. Curcio, M.; De Bonis, A.; Fosca, M.; Santagata, A.; Teghil, R.; Rau, J.V. Pulsed laser-deposited composite carbon–glass–ceramic films with improved hardness. *J. Mater. Sci.* **2017**, *52*, 9140–9150. [[CrossRef](#)]
149. Borrajo, J.P.; Serra, J.; González, P.; León, B.; Muñoz, F.M.; López, M. In vivo evaluation of titanium implants coated with bioactive glass by pulsed laser deposition. *J. Mater. Sci. Mater. Med.* **2007**, *18*, 2371–2376. [[CrossRef](#)]
150. Ma, J.; Chen, C.Z.; Wang, D.G.; Wang, C.Z.; Zhang, H.M. Preparation and apatite formation on CaO-MgO-P2O5-SiO2 glass film grown by pulsed laser deposition. *J. Non Cryst. Solids* **2013**, *382*, 5–10. [[CrossRef](#)]
151. Ledda, M.; De Bonis, A.; Bertani, F.R.; Cacciotti, I.; Teghil, R.; Lolli, M.G.; Ravaglioli, A.; Lisi, A.; Rau, J.V. Interdisciplinary approach to cell-biomaterial interactions: Biocompatibility and cell friendly characteristics of RKKP glass-ceramic coatings on titanium. *Biomed. Mater.* **2015**, *10*, 035005. [[CrossRef](#)]
152. Ledda, M.; Fosca, M.; De Bonis, A.; Curcio, M.; Teghil, R.; Lolli, M.G.; De Stefanis, A.; Marchese, R.; Rau, J.V.; Lisi, A. Placenta Derived Mesenchymal Stem Cells Hosted on RKKP Glass-Ceramic: A Tissue Engineering Strategy for Bone Regenerative Medicine Applications. *Biomed. Res. Int.* **2016**, *2016*, 3657906. [[CrossRef](#)] [[PubMed](#)]
153. Wang, D.G.; Chen, C.Z.; Ma, Q.S.; Jin, Q.P.; Li, H.C. A study on in vitro and in vivo bioactivity of HA/45S5 composite films by pulsed laser deposition. *Appl. Surf. Sci.* **2013**, *270*, 667–674. [[CrossRef](#)]
154. Shaikh, S.; Kedia, S.; Majumdar, A.G.; Subramanian, M.; Sinha, S. 45S5 bioactive glass coating on Ti6Al4V alloy using pulsed laser deposition technique. *Mater. Res. Express* **2019**, *6*, 125428. [[CrossRef](#)]

155. Rau, J.V.; De Bonis, A.; Curcio, M.; Schuhladen, K.; Barbaro, K.; De Bellis, G.; Teghil, R.; Boccaccini, A.R. Borate and silicate bioactive glass coatings prepared by nanosecond pulsed laser deposition. *Coatings* **2020**, *10*, 1105. [[CrossRef](#)]
156. Nádai, L.; Katona, B.; Terdik, A.; Bognár, E. Chemical etching of titanium samples. *Period. Polytech Mech Eng.* **2013**, *57*, 53–57. [[CrossRef](#)]
157. Ma, J.; Wang, C.Z.; Ban, C.L.; Chen, C.Z.; Zhang, H.M. Pulsed laser deposition of magnesium-containing bioactive glass film on porous Ti-6Al-4V substrate pretreated by micro-arc oxidation. *Vacuum* **2016**, *125*, 48–55. [[CrossRef](#)]
158. González, P.; Serra, J.; Liste, S.; Chiussi, S.; León, B.; Pérez-Amor, M.; Martínez-Fernández, J.; De Arellano-López, A.R.; Varela-Feria, F.M. New biomorphic SiC ceramics coated with bioactive glass for biomedical applications. *Biomaterials* **2003**, *24*, 4827–4832. [[CrossRef](#)]
159. Borrajo, J.P.; González, P.; Liste, S.; Serra, J.; Chiussi, S.; León, B.; Pérez-Amor, M. The role of the thickness and the substrate on the in vitro bioactivity of silica-based glass coatings. *Mater. Sci. Eng. C* **2005**, *25*, 187–193. [[CrossRef](#)]
160. De Carlos, A.; Borrajo, J.P.; Serra, J.; González, P.; León, B. Behaviour of MG-63 osteoblast-like cells on wood-based biomorphic SiC ceramics coated with bioactive glass. *J. Mater. Sci. Mater. Med.* **2006**, *17*, 523–529. [[CrossRef](#)]
161. Borrajo, J.P.; González, P.; Serra, J.; Liste, S.; Chiussi, S.; León, B.; Carlos Villamarin, A.; Varela Feria, F.M.; Martinez Fernandez, J.; Ramirez de Arellano Lopez, A. Estudio de la citotoxicidad de cerámicas biomórficas de sic recubiertas con vidrio bioactivo. *Bol. Soc. Esp. Ceram. V* **2006**, *45*, 109–114. [[CrossRef](#)]
162. Gu, X.N.; Li, S.S.; Li, X.M.; Fan, Y.B. Magnesium based degradable biomaterials: A review. *Front. Mater. Sci* **2014**, *8*, 200–218. [[CrossRef](#)]
163. Dorozhkin, S.V. Calcium orthophosphate coatings on magnesium and its biodegradable alloys. *Acta Biomater.* **2014**, *10*, 2919–2934. [[CrossRef](#)]
164. Rau, J.V.; Antoniac, I.; Fosca, M.; De Bonis, A.; Blajan, A.I.; Cotrut, C.; Graziani, V.; Curcio, M.; Cricenti, A.; Niculescu, M.; et al. Glass-ceramic coated Mg-Ca alloys for biomedical implant applications. *Mater. Sci. Eng. C* **2016**, *64*, 362–369. [[CrossRef](#)] [[PubMed](#)]
165. Maçon, A.L.B.; Kim, T.B.; Valliant, E.M.; Goetschius, K.; Brow, R.K.; Day, D.E.; Hoppe, A.; Boccaccini, A.R.; Kim, I.Y.; Ohtsuki, C.; et al. A unified in vitro evaluation for apatite-forming ability of bioactive glasses and their variants. *J. Mater. Sci. Mater. Med.* **2015**, *26*, 115. [[CrossRef](#)] [[PubMed](#)]
166. Zhao, Y.; Song, M.; Liu, J. Characteristics of bioactive glass coatings obtained by pulsed laser deposition. *Surf. Interface Anal.* **2008**, *40*, 1463–1468. [[CrossRef](#)]
167. Wang, D.G.; Chen, C.Z.; Yang, X.X.; Ming, X.C.; Zhang, W.L. Effect of bioglass addition on the properties of HA/BG composite films fabricated by pulsed laser deposition. *Ceram. Int.* **2018**, *44*, 14528–14533. [[CrossRef](#)]